Full Length Article

Plasmonic Au NPs embedded Ytterbium-doped TiO$_2$ nanocomposites photoanodes for efficient indoor photovoltaic devices

Venkata Seshaiah Katta [a], Vishnuvardhan Reddy Chappidi [a], Sai Santosh Kumar Raavi [a,b,*]

[a] *Ultrafast Photophysics and Photonics Laboratory, Department of Physics, Indian Institute of Technology Hyderabad, Kandi 502285, Telangana, India*
[b] *Department of Climate Change, Indian Institute of Technology Hyderabad, Kandi 502285, Telangana, India*

ARTICLE INFO

ABSTRACT

Herein, we present an all-inclusive investigation on the effect of plasmonic gold nanoparticles (Au NPs) embedded Yb-doped TiO$_2$ nanostructured photoanode for efficient photovoltaics devices. Optimally doped Yb (0.5 mol%)-TiO$_2$ nanoparticles (NPs) were synthesised by solid-state grinding. Their structural, morphological, optical, and surface properties were evaluated using XRD, Raman spectroscopy, SEM-EDX, UPS, and XPS. Results show that Yb-doped TiO$_2$ NPs form, reducing the rutile phase and shifting the fermi level. After demonstrating the enhanced properties of Yb-doped TiO$_2$ NPs, we introduced single anatase phase nanowire structures for comparison. Dielectric measurements show Yb-doped TiO$_2$ NW's higher conductivity. Plasmon-induced enhancement of light absorption is achieved by implanting Au NPs into Yb-doped TiO$_2$ NW for additional light harvesting. As a proof of concept, optimised Yb-doped TiO$_2$ photoanode DSSC were fabricated and tested under the AM1.5, 1 sun illumination exhibiting photoconversion efficiency (PCE) of 6 %. Devices employing Yb-doped TiO$_2$ NW: Au NPs photoanode exhibited Jsc to 18.8 % mA-cm^{-2} and PCE% to 8 %. Under white LED (1000 LUX) exhibited PCE of 13.9 % for Au/Yb-TiO$_2$ NW photoanode. The electrochemical impedance spectroscopy (EIS) measurements on these devices established the Yb-doped TiO$_2$ NW: Au NPs photoanode based device exhibited the lowest charge transport resistance (R_2:86 Ω) and charge recombination resistance (R_3:20 Ω) which are consistent with the *J-V* characteristics suggesting the potential use of these photoanode for indoor photo-voltaics (IPV) and in general any devices for allied energy and environmental areas of research.

1. Introduction

The advent of smart Internet of Things (IoT) devices in daily life have created a tremendous requirement to find alternative sustainable solutions to power these devices[1–4]. There is a great thrust to develop photovoltaic devices that work well in diffused light conditions, and the research area of indoor photovoltaics has received tremendous impetus recently[5–7]. Organic molecule-based photovoltaic devices, such as dye-sensitized solar cells[8,9], bulk heterojunction solar cells[10,11], and perovskite solar cells[12,13] have been tested for their utility under artificial indoor light. Rare-earth (RE^{3+}) guests and semiconductor hosts are gaining attention for developing photoanodes with good optical and electrical properties. Notably, (RE) doped-TiO$_2$ is widely employed in photovoltaic and photocatalytic applications[14–17]. Optimal semi-conductor materials are essential for photoconversion energy devices to maximize charge transfer efficiency, electrolyte diffusion, dye adsorp-tion, and exciton generation[18,19]. TiO$_2$ semiconductor was widely

recognized as an effective mediator between dye molecules and elec-trodes [20,21]. However, the absorption capabilities were limited to the UV region because of the larger bandgap and defect states in the TiO$_2$ lattice, which inhibits the charge transport abilities. Therefore, TiO$_2$ has been modified with various dopants, including rare-earth metals, noble metal ions, transition metals, semiconductors, etc., to improve the op-toelectronic properties of TiO$_2$ [22–27]. Among them, rare-earth metal dopants showed the greatest potential to tune the TiO$_2$ owing to their 4f-4f intra-band energy transitions, which led to improving the light-harvesting by upconversion/down conversion effects [28,29]. For example, Yb^{3+}-TiO$_2$ (guest–host) has demonstrated an exceptional photoconversion energy efficiency (PCE%)[30,31]. With the doping effect of Yb^{3+}, modifies the defect-sites in the TiO$_2$ lattice by substituting the Ti^{4+} with Yb^{3+}. Thus, increases the number of oxygen vacancies, which facilitates into favorable band structure of TiO$_2$, thereby improving the charge transportation properties and low recombination rate at the photoanode-dye sensitizer interface[32]. Here in this, We

---

used Yb (0.5 mol%)-TiO$_2$ to study the effect of Yb^{3+} on the intrinsic defects of TiO$_2$ lattice, with the intent of enhancing photovoltaic and photocatalytic capabilities[33–35].

Yb^{3+} is less beneficial for UV and visible light energy despite possessing the simplest energy structure. In these cases, integrating noble metals such as Au and Ag NPs into the Yb-TiO$_2$/N719 dye photoanode is a promising technique for enhancing the PCE% of DSSC[36]. It is known that the Au NPs induce a unique interaction between light and electrons on the surface of the metal nanoparticle. The phenomenon known as Local Surface Plasmonic Resonance (LSPR) occurs due to the oscillation of the electron cloud around the Au NPs in reaction to the applied electric field. Plasmonic nanoparticles exhibit substantial light absorption and scattering effects due to forming electric fields around them [37,38]. Indeed, the N719 dye molecules absorb light strongly in the visible spectrum, although their absorption deteriorates with increasing wavelength. Consequently, incorporating Plasmonic Au NPs is a significant step toward enhancing the overall light absorption efficiency, as gold nanoparticles have an extensive optical absorption effect in the visible region and strong optical interaction with the dye molecules[39]. Therefore, by utilizing the inclusive Plasmonic NPs, the resultant absorption coefficient of dye molecules can be improved [40]. Numerous groups have established the advancement of Plasmonic-induced DSSC [41–43]. In recent years, much research has been done on DSSCs containing multiple Plasmonic ions and several structural designs to improve photovoltaic performance[38,44–46]. In addition, the nanowire-structured TiO$_2$ can be replaced in DSSC as the nanowire can exhibit a greater surface-to-volume ratio, facilitating more dye adsorption, charge transport via the direct electron channel, and substantial light-harvesting via scattering effects [47–49]. The synthesized TiO$_2$ NW exhibits with single anatase phase, which is known to be providing the

higher photocatalytic activity[50]. Numerous groups have initiated the development of various nanostructured photoanodes for DSSC. Pawel et al. [51] demonstrated the comparative enhancement in the PCE% of DSSC with the various nanostructures of TiO$_2$, including nanoparticles, nanowires, and nanotubes of TiO$_2$. Furthermore, Huili et al. [23] noticed a 25 % increase in the PCE% of DSSC when a photoanode composed of noble metal (Au and Ag) was embedded in TiO$_2$ nanowires. M Kumari et al. [52] presented the Ag nanofibers embedded in TiO$_2$-based DSSC with 45 % enhancement over pristine TiO$_2$. Therefore, it is highlighted that the solar device efficiency can be improved by adding features such as Plasmonic materials and rare earth fluorescent doping[53–57]. For example, Peng Zhao et al. [58] showed a PCE% of 8.23 % for the Plasmonic DSSC employed with Au NPs decorated core cell structured NaYF$_4$: Yb, Er@SiO$_2$ photoanode. Whereas the NIR light is effectively trapped and converted to visible radiation by the up-conversion of rare-earth materials, this up-conversion is enhanced with the addition of Au NPs by superimposing the LSPR peak with the up-conversion emissions. Similarly, Parthian et al. [59] report an increase in PCE% of 21.3 % of DSSC using NaGdF$_4$: Yb, Er, Fe upconversion NPs and the Plasmonic silver NPs. In this study, we successfully used the synergistic effect of the LSPR effect of Au NPs and the rare-earth-florescent of Yb^{3+} to improve the performance of DSSCs. The summary of relevant literature has tabulated in Table S1. Hence, this study established a Plasmonic DSSC with a novel photoanode consisting of Au NPs embedded Yb^{3+}-doped TiO$_2$ NWs as presented in Scheme 1. Multiple pathways of charge carrier generation and transport can be observed in the model, which explicitly improve the photovoltaic properties. Therefore, in this work, Au embedded Yb-doped TiO$_2$ nanowires (NW) structures photoanode based DSSC was constructed and achieved a PCE of 8 %, which is nearly 50 % higher than the pristine TiO$_2$ photoanode-based DSSC. in fact, no study
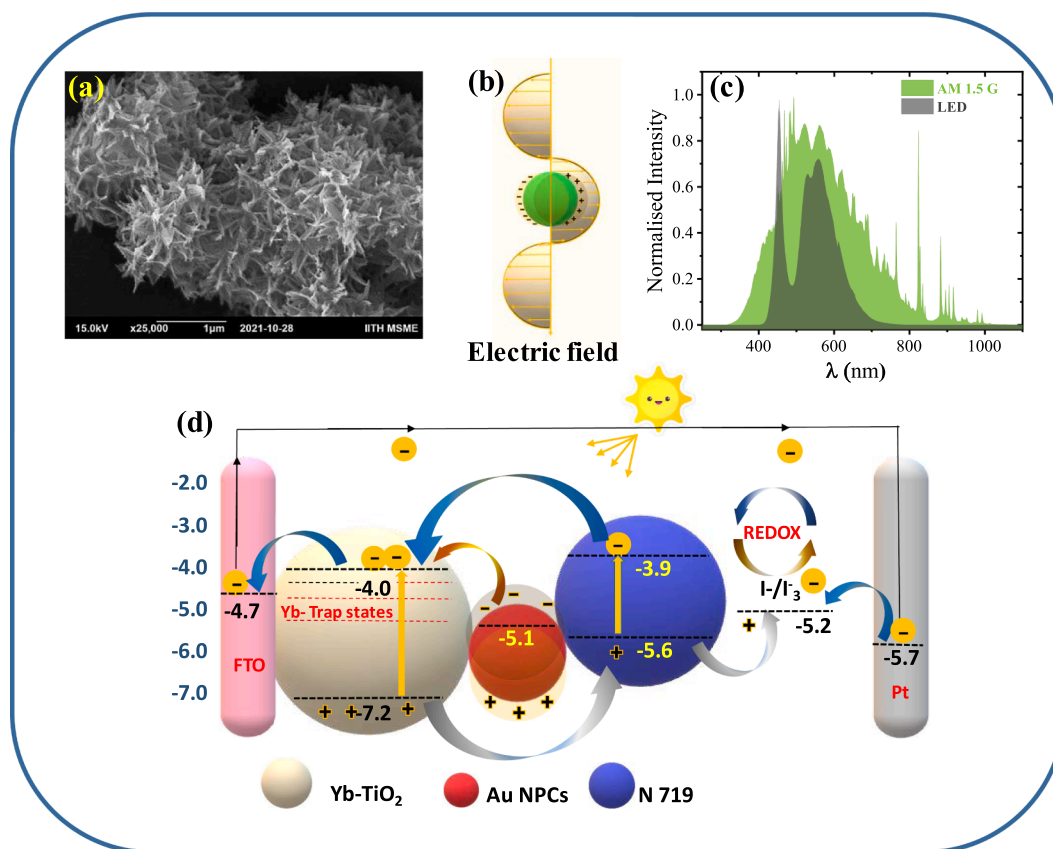
Scheme 1. Schematic representation of the plasmonic Au NPs induced DSSC with Yb-doped TiO$_2$ nanowire cluster structure photoanode under simulated Indoor (LED) light and Outdoor (AM1.5G) light conditions. (a) FESEM images of Yb-doped TiO$_2$ nanowire clusters; (b) schematic representation of Localised Surface Plasmonic Resonance (LSPR) effect; (c) spectral response of White LED light and solar light (Am 1.5G) spectra; (d) schematic representation of Plasmonic induced DSSC working.

has yet been published on the collaborative effort. As a result of DSSC's superior performance in low-light conditions, rather than direct sunlight [9,60,61], this new DSSC design paid attention to the indoor light photovoltaic technology. The research and development has been progressing on the indoor light based photovoltaic technology[30]. Indeed, the IPV system has been successfully used for various solar cell types, including organic photovoltaic (OPV) solar cells[62,63], Perovskite solar cells [12], and DSSC [7]. This work successfully performed the Plasmonic-induced DSSC under indoor light (white LED, 1000LUX). The Yb-doped TiO_2, Au embedded TiO_2, and nanowire clustered structured TiO_2 composite photoanode-based DSSC presents a higher PCE than the pristine TiO_2. In particular, the combined impact of Au NPs implanted Yb-doped TiO_2 NW-DSSC demonstrated a higher PCE (η) of 13.9 %, which is 66 % higher than undoped TiO_2 (η:8.6 %). Thus, the enhanced photovoltaic characteristics of under indoor (ambient) and outdoor (AM 1.5G) light conditions suggest a new path for designing a material combination for collaborative efforts to improve light harvesting. This discovery could pave the way for future research on low-light energy harvesting devices, as recycling indoor light energy could render energy-efficient electronics self-sufficient.

2. Experimental section

2.1. Chemicals

Titanium(IV) dioxide P25 (TiO_2. 99.96 %), Ytterbium (III) oxide ($Yb_2O_3 \cdot 5H_2O$, 99.99 %), 4-*tERT*-BUTYLPYRIDINE ($C_9H_{13}N$, 98 %), Lithium iodide (LiI, 99.9 %), Iodine (I_2, 99.99 %), 1.2-Dimethylimidazolium iodide ($C_5H_9IN_2$, 98 %), and Au NPs colloidal solution (20 nm, 100 %) were purchased from Sigma Aldrich (product no. 741965), N719 (Ruthenium complex, 95 %) dye molecules purchased from Great cell suppliers. Fluorine-doped Tin Oxide (8 Ω/square, LumTec, Taiwan) and Platinum (Pt) coated substrates were purchased from Solronix, Switzerland. Valeronitrile($CH_3(CH_2)_3CN$, 99 %), Acetonitrile (CH_3CN, 99 %), acetylacetone ($C_5H_8O_2$, 99 %), DI water (18.2 MΩ cm^{-1}), Acetone (C_3H_6O, 99 %), Isopropanol (IPA, 99 %), and sodium hydroxide (NaOH, 98 %) pellets were purchased from the SRL supplier.

2.2. Yb-doped TiO_2 NPs synthesis

$Yb_xTi_{1-x}O_2$ synthesis and the photoanode preparation for DSSC were carried out as presented in the literature[64]. The optimal stoichiometry of $Yb_{0.005}Ti_{0.995}O_2$ was prepared through solid-state grinding for eight hours by mortar and pistol. The composition is then transferred to the furnace and annealed for two hours at 500 °C to reduce the composition's stress and hydrocarbon- ions contents. The final product is used for photoanode fabrication.

2.3. Yb- TiO_2 nanowire clusters via solvothermal method

Nanowire clusters were synthesized using the Solvothermal route reported in the literature [60] with few parameter changes. For Yb-doped TiO_2 NWS, solid-state hand-grinded Yb-doped TiO_2 is directly used as a precursor. In contrast, 4 gm of Yb-doped TiO_2 nanoparticles were added to a NaOH solution (10 M NaOH dissolved in 60 ml of DI water) at room temperature while stirring at 500 rpm. The reaction is arrested for more than one hour for homogenous mixing, and then the outcome precipitation is shifted into a 100-ml Teflon-lined autoclave. This autoclave was transferred to an oven and heated to 150 °C for a 24-hr in situ transformation into nanowires. The resultant Yb-doped TiO_2 nanowire clusters were taken out from the autoclave by fleshing the water and then washed with HCL (0.1 mol/L dispersing into 300 ml of DI water) for three hours. After that, the suspension is centrifuged to get a solid sample, and then it washes with DI water repeatedly till the pH value stabilizes to 7. The final composition is dried at 70 °C for 24 hr and then annealed at 500 °C for 30 min to remove the strain attained during the synthesis process.

2.4. Characterization technique

X-ray diffraction spectroscopy (X'PertPRO with Cu K radiation of (=0.15406 nm)) was used to determine the structural characteristics. Additionally, lattice parameters and the cell size were estimated using the Rietveld refinement with FullPof software. Williamson-Hall (W-H) plots were used to estimate the grain size and strain values. Raman spectroscopy (Bruker Senterra dispersive Raman microscope spectrometer with 532 nm) was used to evaluate the molecular structure of the synthesized compositions. Surface analyses of the elemental composition were determined from XPS (Axis Model, Schimadzu) and FESEM-EDX (JEM 2100). Crystallite size and distribution were analyzed using TEM (JEOL F 200 COLD FEG-TEM), and further averaging the crystallite size by ImageJ software. The dielectric measurements were performed using the Wayne Kerr 6500B impedance analyzer over a frequency range of 1 Hz to 1 MHz on the pellet form compounds (pellet preparation S_3). UV–Visible spectroscopy (UV3092, LAB INDIA) was used to determine the optical absorption properties and calculate the bandgap values using Tauc-plot. UPS (Axis Model, Schimadzu) analysis determines the molecular orbital energy in the valance band. PL (FLS 1000, Edinburgh Instruments), and the Time-resolved Photoluminescence (TrPL) were performed using the Time correlated single photon counting (TCSPC) technique. Using a class AAA science tech solar simulator, the current density (*J*) versus potential (*V*) under (AM 1.5G, 1000 W/m^2) was measured for the constructed DSSC, and a white LED (1000 LUX) light source was used for the IPV technology.

2.5. DSSC construction

FTO substrates were cleaned by sonicating with a series of solvents such as soap solution, DI water, acetone, Isopropanol for 15 min each. The cleaned substrates were masked with Scotch tape before film fabrication. The synthesized Yb-doped TiO_2 nanoparticles are converted into a paste by mixing with Triton-X and an acetylacetone-DI water binder (85 % −15 %). The mixture was ground for 30 min using a mortar and pestle for a homogeneous paste. The doctor-blade technique was used to fabricate thin films, which were then subjected to a 15-min heat treatment at 70 °C and annealed at 500 °C for 30 min. Similarly, a second layer is deposited on top of it and then heated to 70 °C for 30 min, followed by annealing at 500 °C for 30 min. The films were further treated with $TiCl_4$ for 30 min at 70 °C to attain nonporous film, annealing at 500 °C for 30 min. Furthermore, 0.5 % M of gold nanoparticles were added to the Yb-TiO_2 paste during the pasting phase to evaluate the LSPR effect of gold nanoparticles on Yb-TiO_2 films. The films were then immersed in N719 dye for 12 hr, and the unadsorbed dye molecules were removed with acetonitrile devoid of water. The fabricated thin films served as photoanodes for the DSSC. TiO_2 deposited FTO substrate (working electrode) and platinum (counter electrode) are stacked using a surlyn polymer for DSSC construction. The electrolyte is composed of DMPII (1 M), I_2 (0.03 M), TBP(0.5 M), and LiI(0.05 M) dissolved in acetonitrile, which was injected into a device through a hole created on the back side of the counter electrode and sealed with thin glass sheet via heat treatment after electrolyte injection.

3. Results and discussion

3.1. Structural, optical and morphological properties of TiO_2 and Yb-TiO_2 nanoparticles

3.1.1. XRD

The phase purity and structural features of TiO_2 and Yb-doped TiO_2 were investigated using X-ray diffraction. The diffracted peaks for the TiO_2 are identified to be {101}, {103}, {004}, {112}, {200}, {105}, {211}, {204}, {116}, {220}, {215} at the position of 2θ: 25.33°,

37.1°, 37.99 °, 38.63 °, 48.25 °, 54.16 °, 55.30 °, 62.86 °, 69.09 °, 70.49 °, and 75.33 °, respectively, indicating the anatase phase. Few low intense peaks are identified at 2θ: 27.57 °, 36.06 °, 41.36 °, 44.17 °, 56.79 °, and 62.88 ° that can be attributed to the lattice planes of {1 1 0}, {1 0 1}, {1 1 1}, {2 1 0}, {2 2 0}, and {0 0 2} respectively, which belongs to the rutile phase. Thus, the resultant XRD pattern of (P 25) reveals a dual phase of anatase and rutile phase, as depicted in Fig. 1(a). The resultant anatase and rutile phase were well matched with the standard data file (JCPDS 21-1272) and (JCPDS 21-1276), respectively. No additional peaks related to impurities or the second phase of Yb were detected in Yb-doped TiO_2. Significant phase matching with the XRD pattern of TiO_2 suggests that the Yb^{3+} dopant is effectively incorporated into the TiO_2 lattice[65]. Indeed, there is a negligible phase shift in the XRD pattern due to Yb-doping, as seen in Fig. 1(b), which may indicate the lattice deformation of TiO_2 caused by the substitution of Ti^{4+} with Yb^{3+}. Furthermore, Rietveld refinement is accompanied on the XRD of Yb-doped TiO_2 to evidence the site replacement of Ti^{4+}-ion with the Yb^{3+}-ion. Fig. 1(c-d) demonstrates that the calculated XRD profile and observed data for undoped TiO_2 and Yb-doped TiO_2 were in good agreement. The calculated structural parameters are tabulated in Table 1. These structural modifications may lead to a reduction in strain and lattice constant[66]. Under Yb-doping into TiO_2, observed the reduction in the lattice parameter of "a" and "c", where the reduced "c" parameter indicates the compression strain existence in the TiO_2 lattice [67]. The volume of the lattice cell is reduced to 135.88 $(A°)^3$ from 136.05 $(A°)^3$ for Yb-doped TiO_2. The reduced lattice cell of Yb-TiO_2 would signify the site substation of Ti^{4+} with the higher ionic radius of Yb^{3+}. When Yb-ions are incorporated into TiO_2, the production of Yb-Ti-O and Yb-O bonds is possible. This formation of new bonds could

Table 1
XRD profile structural parameters obtained from the Rietveld refinement on the XRD pattern of TiO_2 and Yb-doped TiO_2. "lattice parameters (a,b,c), and unit cell volume (V)".

TiO_2	Yb-doped TiO_2
Anatase phase	**Anatase phase**
a = b = 3.783 A°	a = b = 3.782 A°
c = 9.507 A°	c = 9.500 A°
V = 136.05 $(A°)^3$	V = 135.88$(A°)^3$
Rutile phase	**Rutile phase**
a = b = 4.592 A°	a = b = 4.589 A°
c = 2.958 A°	c = 2.954 A°
V = 62.37$(A°)^3$	V = 60.20$(A°)^3$
Anatase (wt.%) = 92.97 % +	**Anatase (wt.%) = 97.25 % +**
Rutile (wt.%) = 7.03 %	**Rutile (wt.%) = 2.75 %**
R_p = 7.17	R_p = 12.5
R_{wp} = 9.92	R_{wp} = 14.1
χ^2 = 3.6	χ^2 = 2.85
Grain size = 39.9 nm	Grain size = 33.8 nm
Strain = 0.0034	Strain = 0.0020

stabilize the Ti-O bond, whereas the breakage of the Ti-O bond is required for grain growth/suppression. Hence, the phase transition and crystal growth are impeded[68]. Furthermore, when Yb^{3+} is substituted for Ti^{4+}, there will be a lattice distortion of TiO_2 since Yb^{3+} has a larger ionic radius (1.0 Å) than Ti^{4+} (0.6 Å), and this may have contributed to the formation of interstitial titania, all these effects could lead to supress the phase transition from anatase to rutile[69]. This suppression of phase transition under Yb-doping suggests grain inhibition since it is well known that the grain size of anatase phase TiO_2 is less than that of rutile phase TiO_2. Rietveld refinement analysis demonstrates the rutile
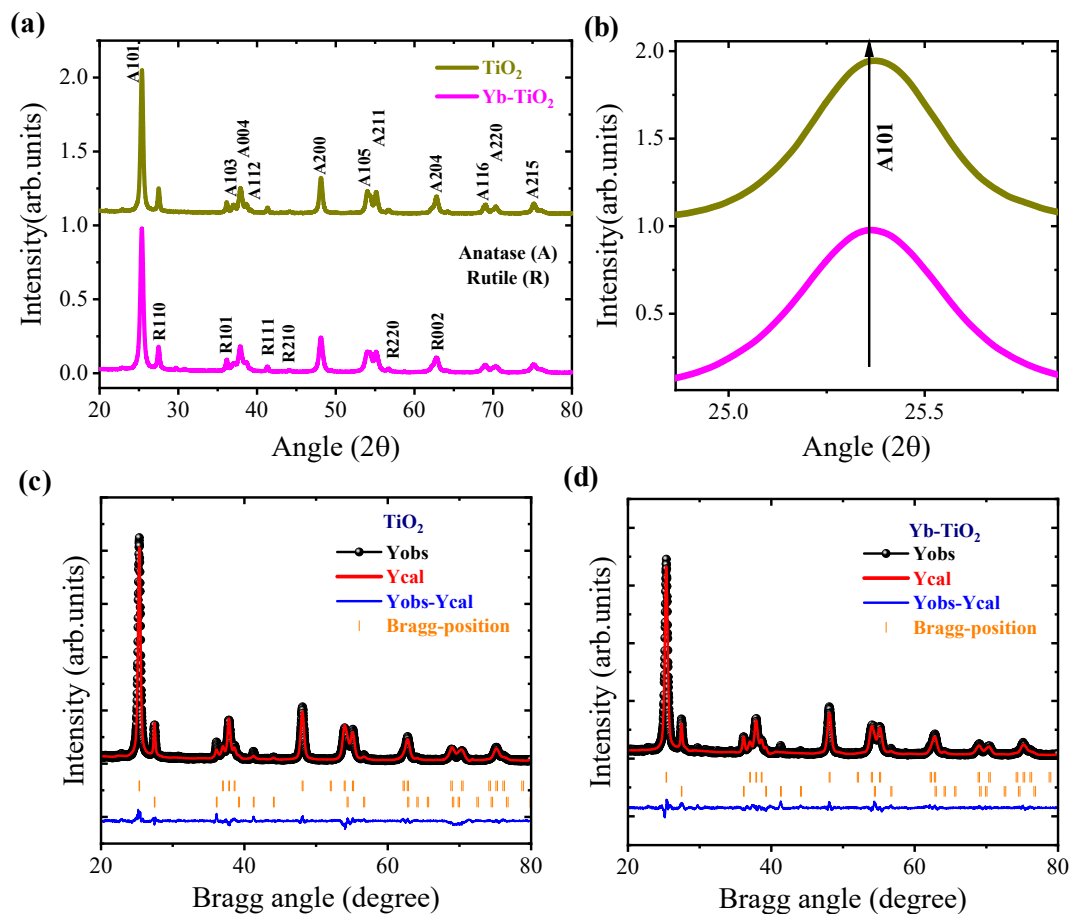

Fig. 1. (a) XRD comparison between Yb^{3+} doped TiO_2 and undoped TiO_2, (b) XRD peak (A101) shift representation, (c-d) Rietveld refinement quantitative analysis of XRD pattern of pristine TiO_2 and Yb-doped TiO_2.

phase decrease in the mixed-phase of TiO_2 under Yb-doping impact.

Williamson-Hall (W-H) plots distinguish the grain size and micro-strain for TiO_2 and Yb-doped TiO_2 under the following equation of $\beta cos\theta = C\varepsilon sin\theta + (K\lambda/D)$ where ε is indicating the strain and D is the grain size (crystallites), the corresponding W-H plots presented in supporting information S_1. Yb-doped TiO_2 has smaller crystallites and less strain than TiO_2, as shown in Table1. In fact, small crystallites have an excellent surface-to-volume ratio, resulting in increased dye adsorption, which is essential for optoelectronic devices.

3.1.2. Raman spectroscopy

Raman spectroscopy was used to study the vibrational modes of Yb-doped TiO_2 and pristine TiO_2, as shown in Fig. 2(a). The Raman spectra of TiO_2 display Raman peaks at 142, 392, 515, and 635 cm^{-1}, which corresponds to the vibrational modes of symmetric stretching (E_g), and symmetric bending (B_{1g}), and anti-symmetric bending (A_{1g}), respectively. The Raman spectra of Yb-doped TiO_2 were observed to be similar to undoped TiO_2, indicating that the addition of doping elements does not influence the lattice structure of TiO_2[34]. On the other hand, a slight phase shift was observed in the Yb-doped TiO_2 towards a longer wavelength, as shown in Fig. 2(b). there is quenching observed in the Raman peak intensity as a result of Yb doping, which is ascribed to the distorting of the Ti^{4+} centre and the formation of Ti^{3+} defects[70]. Thus, these results suggest that the Yb is effectively incorporated into the TiO_2[71]. Indicating low crystallinity, which is consistent with the XRD analysis.

3.1.3. X-ray photoelectron spectroscopy (XPS)

The chemical analysis of the surface of Yb-doped TiO_2 and undoped TiO_2 samples was investigated using XPS. Fig. 3(a) depicts the XPS wide-scan spectrum, which distinguishes the available Ti (2P), O (1s), and C (1s) elements in TiO_2. In comparison, the Yb-doped TiO_2 displays a survey spectrum similar to the reported TiO_2. The Yb^{3+} elements enabled to detect over182.1 eV region in the wide-scan spectrum indicate that Yb's formation on the surface of TiO_2 is significantly low. Fig. 3 (b) depicts the high-resolution XPS spectrum of Ti 2P, representing spin–orbit doublets of Ti $2P_{1/2}$ at 464.5 eV and Ti $2P_{3/2}$ at 458.85 eV, which correspond to the Ti^{4+} oxidation state of TiO_2. Likewise, Yb-doped TiO_2 exhibits similar Ti 2P spectra to those of undoped TiO_2 with a slight peak shift towards lower binding energy. The shifted spin–orbit doublets were identified at 457.5 eV (Ti$2P_{1/2}$) and 463.5 eV (Ti$2P_{3/2}$), which may attribute to the Ti^{3+} oxidation state of TiO_2 [70].

As depicted in Fig. 3(c), the O 1s of both undoped TiO_2 and Yb-doped TiO_2 exhibit an asymmetric and widening spectrum. The O 1s orbital spectrum represents a strong peak at 530.05 eV, which corresponds to the Ti-O bond, and the other peak is identified at 531.8 eV, representing the hydroxyl oxygen groups. The peaks were highlighted with the Gaussian peak fitting. In contrast, Yb-doped TiO_2 exhibited a phase shift in the O 1s orbital spectrum towards lower binding energy. The study indicates that the binding energy of Ti 2P orbital and O 1s orbital are reduced for Yb-doped TiO_2, indicating the formation of new chemical bonds between the Ti and Yb elements[72].

3.1.4. UV–Visible absorption spectroscopy

UV–vis absorption spectra were carried out to evaluate the optical absorption properties of undoped and Yb-doped TiO_2 compositions in Diffused Reflection Spectroscopy (DRS) mode. As illustrated in Fig. 4(a, inset), the optical edge of Yb-doped TiO_2 is redshifted, suggesting the extended absorption ability. Tauc plots with Kubelka Munk (K-M) function were employed to determine the band gap of the samples, as shown in Fig. 4(b). It was observed that the bandgap of Yb-doped TiO_2 is narrower than that of undoped TiO_2, probably due to trap-site alteration in TiO_2 by incorporating the Yb-intra-band states. Moreover, oxygen vacancies and Ti^{3+}- oxidation states may develop when Yb^{3+} replaces Ti^{4+}. Creating these additional states below the conduction band would cause the conduction band's edge to slip down. This engineered TiO_2 with a narrower bandgap improves absorption and charge injection via enhancing Ohmic contact. Formation of these additional states could improve photo-excited electron charge hopping. Thus, the charge recombination is expected to be low. UPS analysis was used to consolidate the Yb-doped TiO_2 band structure results.

3.1.5. Ultraviolet photoelectron spectroscopy (UPS)

UPS is carried out to investigate the influence of Yb dopant on the changes in the band structure of Yb-TiO_2. Fig. 5(a) illustrates the UPS of TiO_2 and Yb-doped TiO_2. Work function (ϕ) can be determined by deducing the secondary electron cut-off ($E_{cut-off}$) from the excitation energy (hϑ) of He I (21.22 eV). Accordingly, the ϕ can be expressed as $\phi = h\vartheta - (E_{cut-off})$ [73]. Whereas, $E_{cut-off}$ is obtained by extrapolating the higher binding energy edge intersection with UPS background as presented in Fig. 5(b). The work function of Yb-TiO_2 is calculated to be 4.11 eV, which is 0.2 eV larger than TiO_2 (3.91 eV), as shown in Table 2. This improved work function may be attributable to the substitutional replacement of Ti^{4+} with Yb^{3+}. Over the doping effect of Yb, there is a chance of forming the defect sites below the conduction band minima (CBM), which may belong to the impurity or second phase elements of Yb^{3+} energy states, thereby, fermi level shift occurred towards the valance band. Furthermore, ionization (E_I) energy and electron affinity (E_a) were estimated by following the equation of $E_I = \phi + E_{VBM}$, and $E_a = E_I - E_g$, whereas the valence band maxima (E_{VBM})was obtained by extrapolating the low binding energy edge intersecting with the X-axis
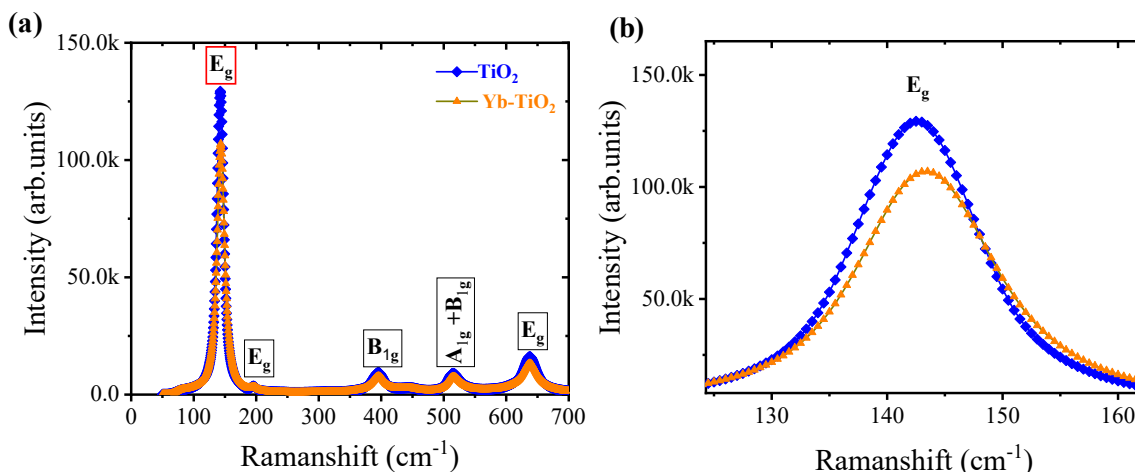

Fig. 2. (a) Raman spectra of Yb-doped TiO_2, and undoped TiO_2, (b) Raman peak (142 cm^{-1}) shift identification.
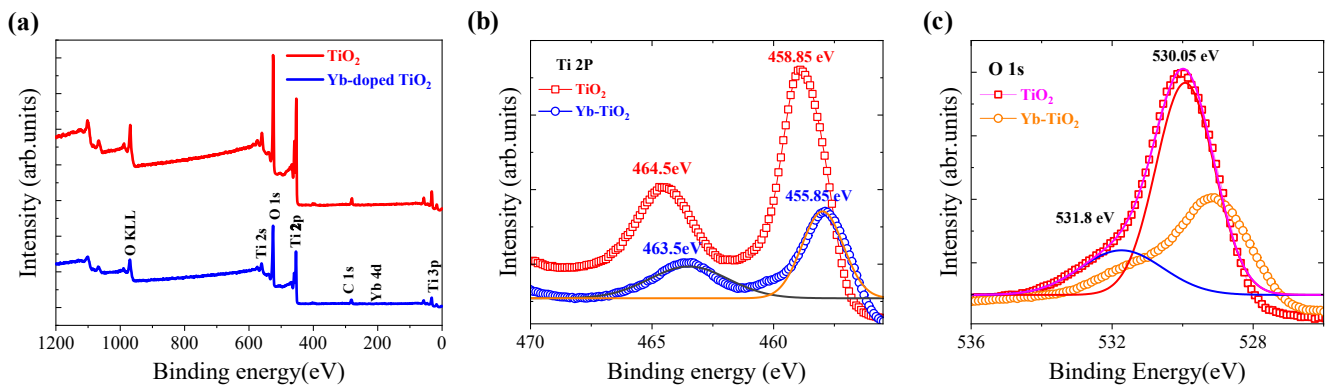
Fig. 3. XPS surface analysis. a) Wide-scan spectrum, (b-c) high-resolution XPS spectrum of Ti 2P and O 1s.
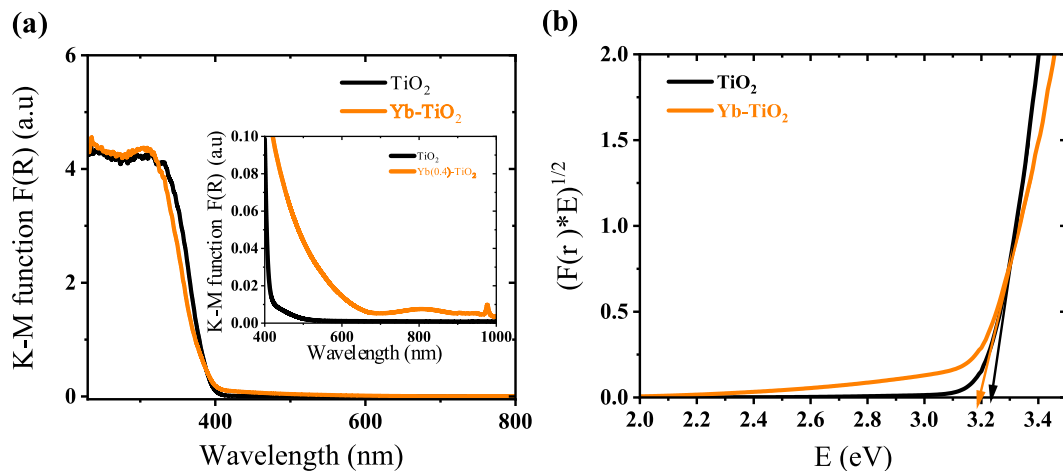

Fig. 4. (a) UV–visible absorption spectra in DRS mode (inset: absorption edge & Yb- related absorption peak at 980 nm) (b) Kubelka Munk plot for bandgap calculations of undoped TiO_2 and Yb-doped TiO_2.

as depicted in Fig. 5(c) [74] and E_g representing the bandgap of the sample as estimated by Tauc plots. Fig. 5(d) depicts the band-diagram for pristine TiO_2 and Yb-doped TiO_2 using all the calculated energy states. The band diagram reveals that the energy difference between the CBM and E_f is enlarged in the Yb-doped TiO_2, and the difference (CBM-E_f) is about 0.42 eV. This results can be relating to the formation of shallow/deep trap-states at below the conduction band. These trap-states are fundamentally crucial for charge transport and recombination effects. If the trap-site distribution range is near the CBM, the trap states are considered shallow traps. These trap states facilitate charge transport by enhancing the charge hopping mechanism[75]. Therefore, Yb-doped TiO_2 serves as an effective Electron Transport Layer (ETL) for the DSSC due to its enhanced charge transport capabilities. Indeed, the downshifted VBM implemented a built-in potential that enhanced charge migration at the interface. Then, Yb-doped TiO_2 is expected to have better charge transport and injection capabilities. The PL investigations add to evidence of improved charge transport and injection capabilities.

3.1.6. SEM and TEM images

Scanning Electron Microscopy (SEM) is performed on pristine TiO_2 and Yb-doped TiO_2 powder samples to investigate the morphological properties. TiO_2 exhibits a variety of particle sizes and shapes, as seen in Fig. 6(a-b). Spherical-shaped particles range in size from 10 nm to 60 nm, while nanorod-shaped particles range in length from 50 nm to 150 nm. Histogram plots display the particle size distribution, and the average particle size was 41 nm. The SEM image of Yb-doped TiO_2 shows smaller particles with an average size of 33.5 nm. It is usually

believed that bigger particles impose a high degree of crystallinity. Thus, Yb-doped TiO_2 has low crystallinity, and these values were consistent with the XRD plots. Furthermore, Transmission Electron Microscopy (TEM) was performed for better insight into the morphological properties, as shown in Fig. 6(c-d). As seen in the SEM images, TiO_2 crystallites came in various sizes and shapes. Crystallites range from 10 nm to 100 nm, averaging 37.4 nm. For Yb-doped TiO_2, the average crystallite size is 33.4 nm, and most of the crystallites were monitored in the range of 20 to 30 nm. Crystallite sizes calculated from TEM images agreed with those observed by XRD. In addition, they are measuring the selective area electron diffraction (SAED) pattern, as shown in Fig. 6(e-f). The displayed diffracted fringes of the Yb-doped TiO_2 and undoped TiO_2 samples illustrate the existence of poly-crystallinity. The phase purity and the structural existence can be distinguished using the diffracted fringes obtained from the SAED pattern. TiO_2 is identified with the lattice plans of{1 0 1}, {1 1 2}, {2 0 0}, and {2 1 1} based on the d-spacing values that have been determined from SAED pattern. The existing lattice plans indicate the presence of the anatase phase in the sample, and the additional {0 0 2} referring the rutile phase. Thus, the lattice fringes suggest that the TiO_2 contains anatase and rutile phases. The intensity of spots from Bragg reflection is reduced in the SAED pattern of Yb-doped TiO_2, suggesting the low crystallinity due to the doping effect. In summary, the obtained diffracted rings of TiO_2 and Yb-doped TiO_2 are well-matched with the XRD pattern.

3.2. Yb-doped TiO_2 nanowires

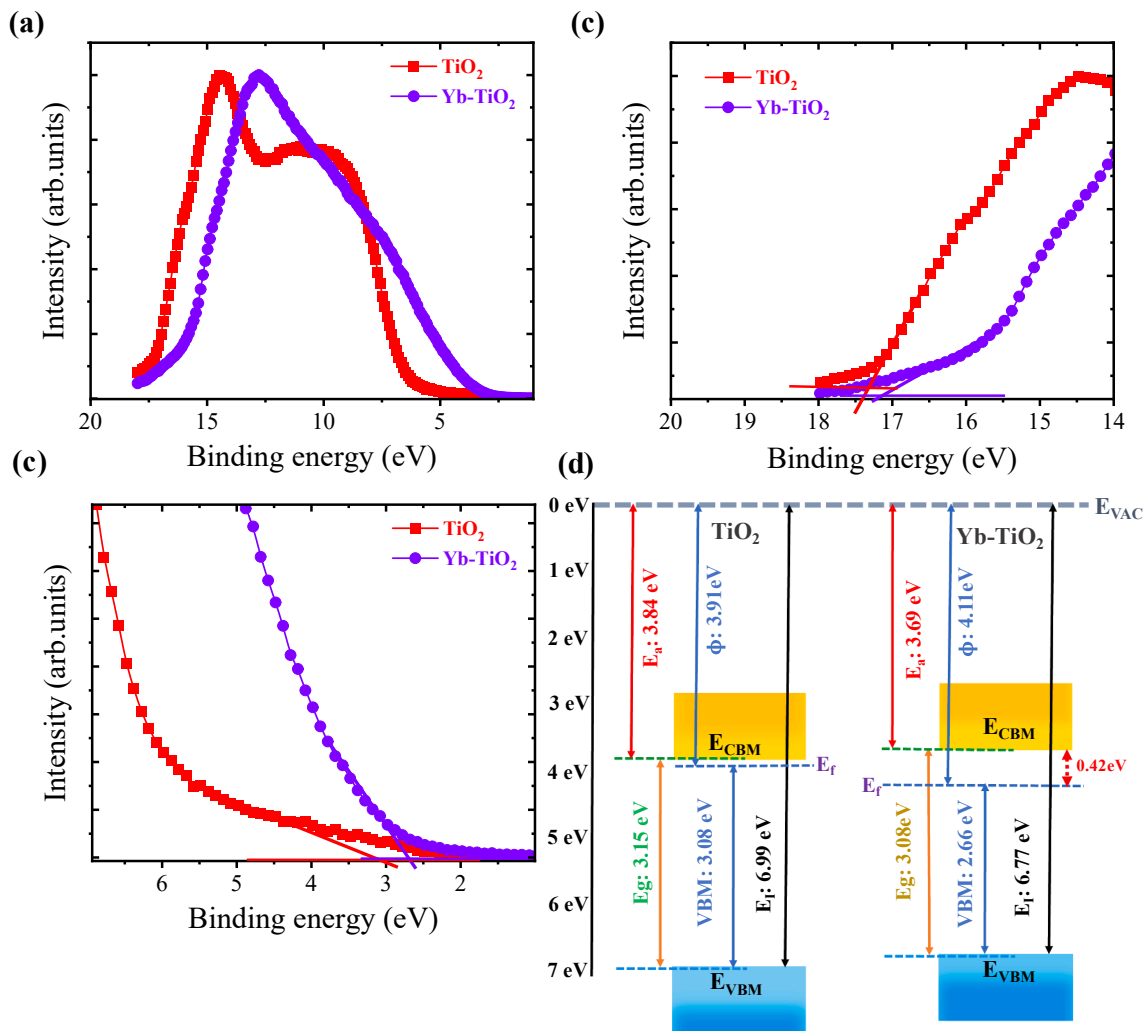Fig. 7(a-b) presents the SEM images of Yb-doped TiO_2 NW at

Fig. 5. (a) Ultraviolet photoelectron spectroscopy (UPS) analysis, (b) magnified view of secondary electron cut-off region (SECO), (c) valance band edge of undoped TiO_2, and Yb-doped TiO_2, and (d) band-diagram for pristine TiO_2 and Yb-doped TiO_2.

Table 2
Calculated energy values of pristine TiO_2 and Yb-doped TiO_2 from UPS analysis.

sample	$E_{cut-off}$	E_{VBM}	ϕ	E_I	E_a	E_g	$E_f - CBM$
TiO_2	17.31	3.08	3.91	44 nm	3.84	3.15	0.07
Yb-TiO_2	17.11	2.66	4.11	41 nm	3.69	3.08	0.42

different magnifications. Here, a straightforward solvothermal approach converted the solid-state synthesized Yb-doped TiO_2 NPs into nano-wires. Fig. 7(a) represents the SEM image, which resembles nano flowers or flakes. However, clusters of nanorods and nanowires can be observed in Fig. 7(b) when the image is zoomed in even more. The following equation depicts the formation of TiO_2 NWs during solvothermal treatment.[76].

$$3TiO_2 + 2NaOH = Na_2Ti_3O_7 + H_2O$$

$$Na_2Ti_3O_7 + 2HCl = H_2Ti_3O_7 + 2NaCl$$
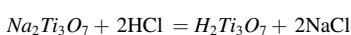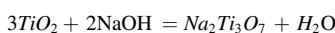
After annealing the $H_2Ti_3O_7$ at 500 °C, all the hydrogen and additional oxygen ions are exempted, and then the TiO_2 anatase phase can be observed, as illustrated below.

$$H_2Ti_3O_7 = 3TiO_2 + H_2O.$$
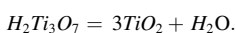
The structural properties of undoped TiO_2 NWs and Yb-doped TiO_2

NWs were evaluated using the X-ray diffraction pattern shown in Fig. 7 (c). The XRD pattern of undoped TiO_2 NW exhibited a single anatase phase, which was well matched with the standard data file (JCPDS 21-1272). The XRD pattern of Yb-doped TiO_2 was identical to that of undoped TiO_2, showing that the solvothermal technique successfully introduced Yb into the TiO_2 lattice. In contrast to the TiO_2 NPs, the rutile phase has completely nucleated in the TiO_2 NW (supporting information S_2). These findings could be ascribed to the few atoms in the anatase lattice plane, which may produce nucleation sites for the rutile phase. [77]. In addition, the acid treatment that takes place during the sol-vothermal synthesis has the potential to nucleate the rutile phase of TiO_2 NW[78]. Furthermore, the elemental compositions of the materials were determined using the EDX spectrum, which is shown in Fig. 7(e-f). The EDX spectrum of TiO_2 reveals the elemental compositions of Ti and O, with no other impurity-related peaks found. Yb-doped TiO_2 yields a strong Ti peak and O peaks with few Yb^{3+}-peaks. According to the quantitate analysis, Yb(III) has a stoichiometric doping percentage of (0.5 % mol), demonstrating the presence of Yb-peaks under ideal doping conditions.

3.3. Dielectric properties

The dielectric measurements were carried out for the undoped TiO_2, Yb-doped TiO_2 nanoparticles, and Yb-doped TiO_2 nanowire composi-tions over a frequency range from (1000 Hz to 10 MHz) at ambient
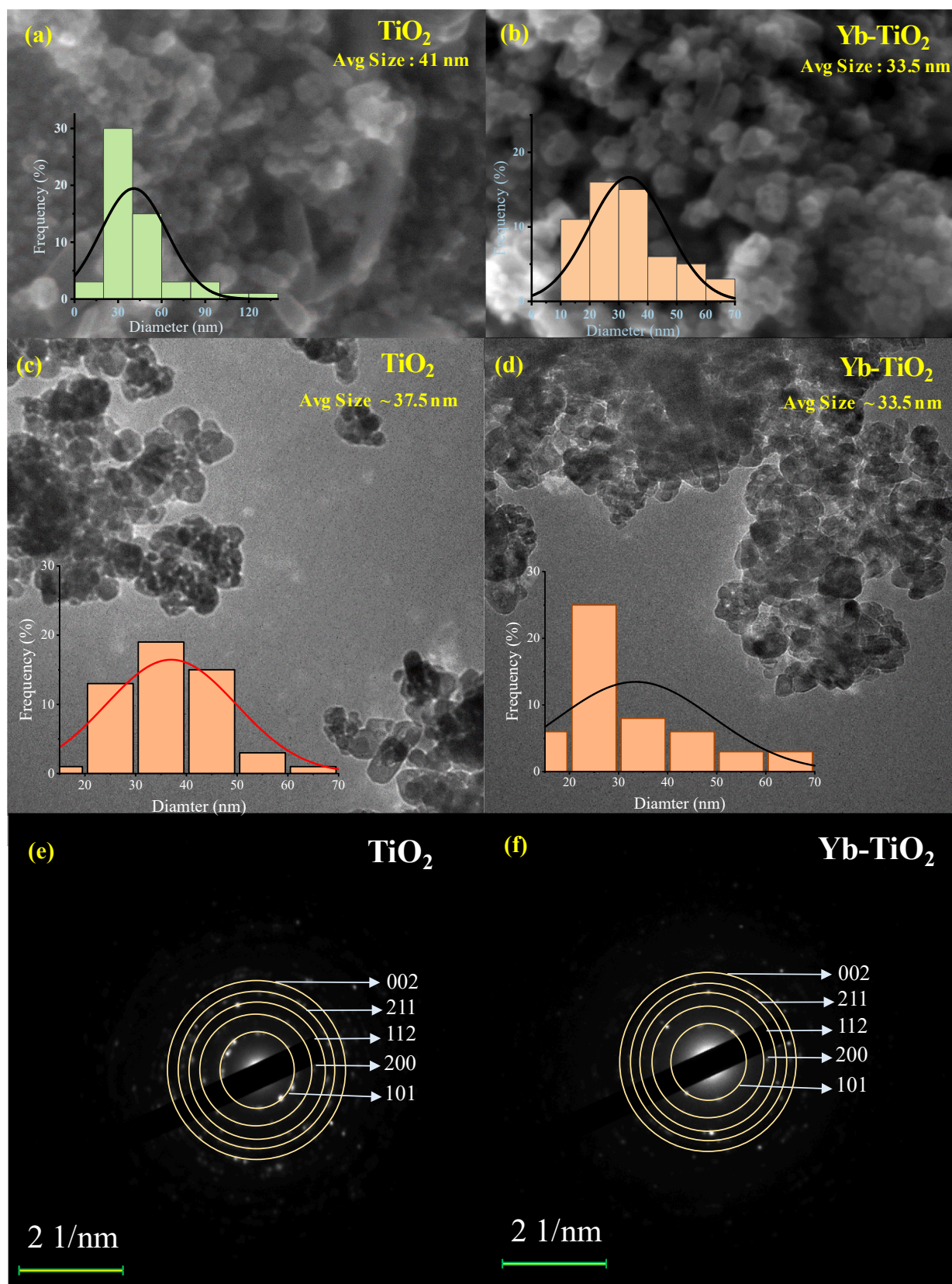
Fig. 6. (a-b) SEM images, (c-d) TEM images of pristine TiO_2 and Yb (0.5 M)-TiO_2 compounds (inset: histogram of the particle's diameter distribution), and (e-d) selective area electron diffraction (SAED) patterns of TiO_2 and Yb-doped TiO_2.
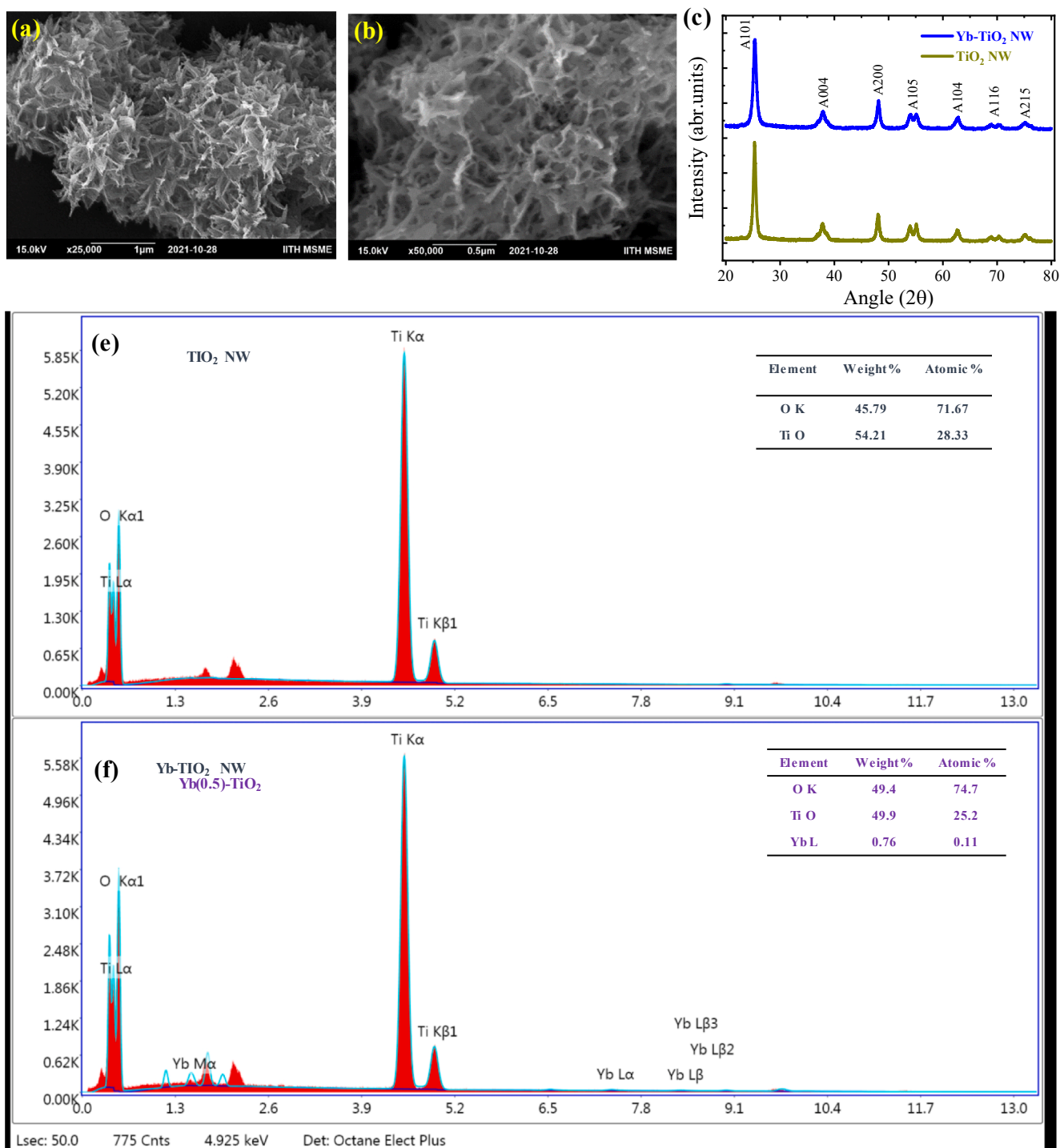
Fig. 7. (a-b) FESEM images of Yb-doped TiO$_2$ nanowire clusters (NWs) at different magnifications, Fig.(c) XRD pattern for pristine TiO$_2$ NWs and Yb-doped TiO$_2$ NWs synthesized via solvothermal route, and (e-f) Elemental compositions of TiO$_2$, and Yb-doped TiO$_2$ NW.

conditions. The polarization of the dielectric material can be determined by the dielectric constant (ε'), estimated using the relation of $\varepsilon' = Cd/\varepsilon_o A$. Where ε_o indicates the permittivity of free space, C denotes the capacitance, d represents the thickness, and A denotes the pellet area. Fig. 8(a) displays the variation in the dielectric constant(ε') under a frequency range from 1000 Hz to 10 MHz. It has a higher dielectric constant at lower frequencies and gradually decreases as the frequency increases. The dielectric behavior of the material is determined based on the Maxwell–Wagner interfacial type of polarization. According to this model, the decrease in dielectric constant as frequency increases is attributed to the formation of insulating grain boundaries around the grains. This phenomenon indicates that polarizability's effect is decreasing within the grain. Consequently, the dielectric properties diminish as frequency increases. As a result, it is clear that grain boundaries actively influence the (ε'), notably at low-frequency ranges. This higher ε' at lower frequency ranges can be attributed to space charge polarisation. On the other hand, grains can actively influence the ε' at midrange frequency, which is attributable to the dipole polarization relaxation. Since the grain size of the Yb-doped TiO$_2$ is smaller than undoped TiO$_2$ (evaluated from XRD), which introduces more grain
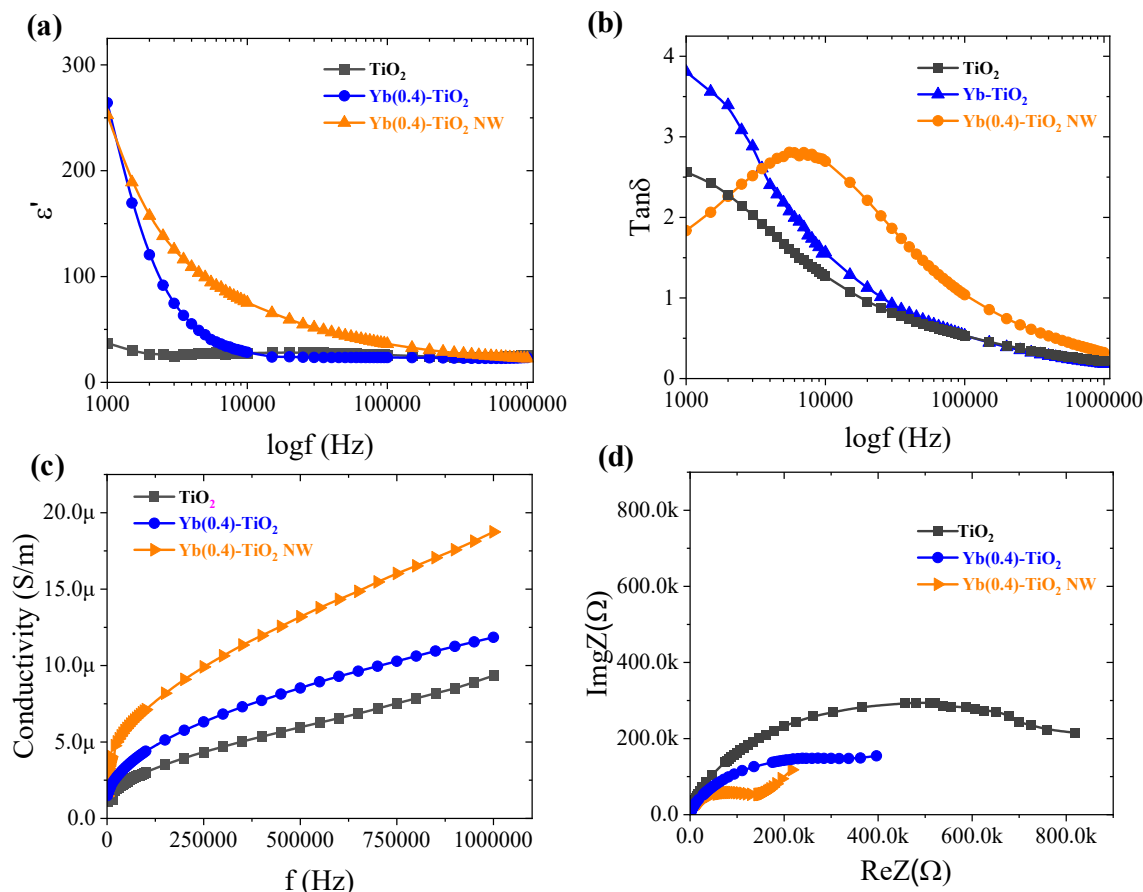
Fig. 8. (a) dielectric permittivity, (b) dielectric tangent loss, (c) electric conductivity, and (d) Nyquist plot of undoped TiO$_2$, Yb-doped TiO$_2$, and Yb-doped TiO$_2$ NW compositions under a frequency range of (1000 Hz to 10 MHz) at room temperature.

boundaries in the samples, thereby exhibiting the higher dielectric constant at a lower frequency regime. This study showed a sixfold enhancement in the dielectric constant for Yb-doped TiO$_2$ than pristine TiO$_2$ NPs at 1000 Hz. This enhanced dielectric constant is also attributed to the grain boundary defects and oxygen vacancies[79]. As mentioned earlier, oxygen vacancies are expected to form when Ti^{4+} replaces the Yb^{3+} oxidation state in Yb-doped TiO$_2$. Indeed, the dielectric constant can be attributable to the ability of electron hopping in the material[80]. The greater the number of electrons, the longer the hopping distance. Therefore, as a result of the oxygen vacancies present in Yb-doped TiO$_2$, the dielectric constant is substantially enhanced. Among all the samples, Yb-doped TiO$_2$ NW exhibits dielectric decay throughout the frequency range from 1KHz to 1 MHz, indicating the high polarise sensitivity.

Furthermore, the dielectric tangent loss was estimated using the equation of $\varepsilon'' = \varepsilon' \tan\theta$. As seen in Fig. 8(b), the dielectric loss (tanθ) exhibits a similar trend as ε' has demonstrated. Yb-doping enhanced dielectric loss at 10^4, which can be attributed to the enhancement in the electric conductivity as the pace of charge conduction is responsible for the dielectric loss. Additionally, charge carrier mobility was evaluated using conductivity (σ) measurements, which account for electron transport abilities between grains and grain boundaries. Fig. 8(c) depicts the variations in the electric conductivity under the applied frequency. As frequency increases, conductivity increases, showing that the charges were mobilized in the presence of an electric field. Yb-doped TiO$_2$ NW exhibited a threefold increase in conductivity when compared to pristine TiO$_2$. Furthermore, the Nyquist plot (Z'' vs Z'). was shown with the relevant frequency at ambient temperature. Fig. 8(d) illustrates the Nyquist plot with two semicircular arcs. The smaller semicircular arc at low frequencies is associated with grain boundary resistance effects, whereas the large semicircular arc at high frequencies is associated with

grain resistance. The smallest semicircular arcs were observed for Yb-doped TiO$_2$ NW, indicating increased charge conductivity at the grain boundaries.

In conclusion, the dielectric characteristics were comparable with the effective charge conductance of Yb-doped TiO$_2$ NPs/NWs compared to pure TiO$_2$. Solar cell applications benefit from materials with a high dielectric constant and electric conductivity.

3.4. Localized surface plasmonic resonance (LSPR) effect

The LSPR effect occurs when light strikes the metallic nanostructures. LSPR is a term that refers to the oscillation of an electron cloud surrounding metallic nanostructures. In detail, metallic NPs exposed to an electric field become polarised and behave as dipoles. The dipoles generate the restoring force within the nucleus and act opposite to the applied electric field. When the frequency of the applied electric field is resonant with the size of metallic nanoparticles, the dipoles exhibit the action of restoring force and oscillate with the applied electric field. Fig. 9(a) illustrates the metallic nanoparticles' LSPR effect. To establish the LSPR effect of Au NPs in Yb-TiO$_2$ composites, performed the UV–vis absorption measurements on Yb-doped TiO$_2$ thin-films after adding the Au NPs (0.5 mol %). The Au NPs coated thin film showing the surface Plasmon absorption band at 520 nm, as shown in Fig. 9(b). A comparable Plasmonic band can be observed for the Au NPs embedded Yb-TiO$_2$ thin-film compared to bare Yb-TiO$_2$. Therefore, it is emphasized that with the combined effect of dye absorption and the LSPR absorption band, more photons can be trapped, thereby improving the charge collection. Consequently, it was expected that the photovoltaic properties of Plasmon-induced DSSC would improve.
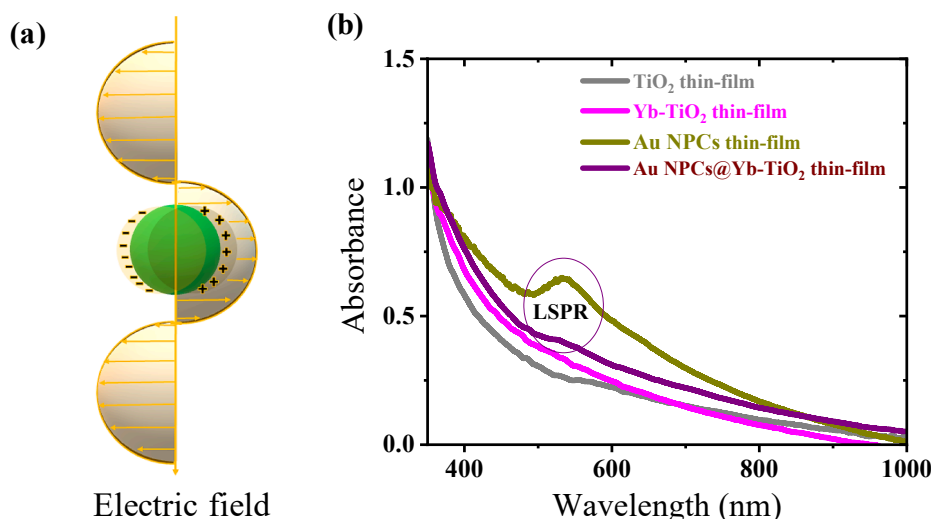
Fig. 9. (a) Schematic representation of Localised Surface Plasmonic Resonance (LSPR) effect, (b) UV–vis absorption spectrum of TiO_2, and Yb-doped TiO_2 thin-film with LSPR absorption band.

3.5. Photoluminescence (PL) emission studies

Photoluminescence (PL) emission analyses were conducted to examine the charge carrier recombination/injection properties of ruthenium dye-loaded TiO_2 films. The ruthenium(N719) dye-loaded TiO_2 shows the PL emission at 720 nm under the excitation of 520 nm, as depicted in Fig. 10(a), which characterizes the recombination of excited e^-/h^+ pair in the dye molecules. The PL intensity of Yb-doped TiO_2/dye is observed to be reduced as compared with TiO_2/dye, this quenching effect indicating the lower recombination of excitons which improves the charge separation. As observed from the UPS analysis, the modified band structure of Yb-doped TiO_2 may improve Ohmic contact with dye molecules. This advantageous interface enhances the charge separation at the interface of dye molecules with Yb-doped TiO_2[23]. Furthermore, with the addition of Au NPs into Yb-doped TiO_2, the PL intensity reduced further, indicating that the charge recombination process has suppressed more under the influence of the Au NPs Plasmonic effect. Notably, the Schottky barrier at the interface between TiO_2 and Au NPs establishes the charge transfer path among them, thereby offering additional quenching in the PL emission. As estimated, the dye-sensitized TiO_2 NW showed lower intense PL emission than TiO_2. Among them, Au-added Yb-doped TiO_2 NW reports a higher quench in the PL emission. It is hypothesized that the combination of Yb-dopant, plasmonic Au NPs, and the nanostructured clusters effectively reduced the recombination process. To better understand, we have performed a Time-resolved Photoluminescence Lifetime (TrPL) upon the excitation of a 505 nm laser diode, as shown in Fig. 10(b). The ruthenium(N719) dye-loaded TiO_2 films present longer lifetime decays. The decay lifetime parameters were estimated using the Fluoracle software and tabulated in Table 3. The TrPL decay values are observed to become shorter for the engineered TiO_2, suggesting the improved charge injection from dye molecules. Particularly, Yb-TiO_2 NW: Au photoanode reported effective charge injection abilities. Subsequently, Yb-doped TiO_2 NW: Au –based

Table 3
TrPL fitting parameters of N719 dye sensitised TiO_2 and doped TiO_2 thin-films.

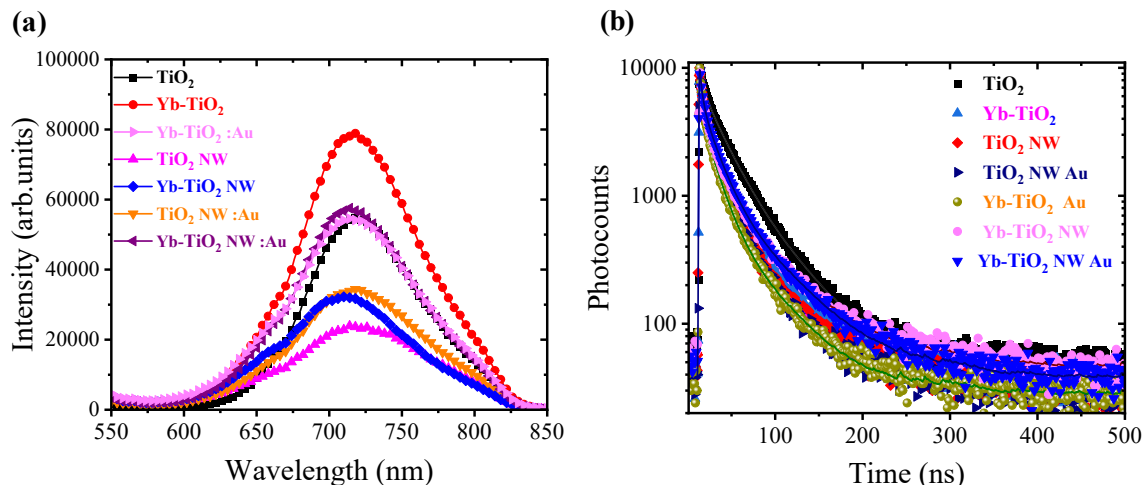| Photoanode	τ_1(ns)	τ_2(ns)	τ_3(ns)	χ^2
TiO_2	4	23	50	1
Yb-TiO_2	4.4	17.4	58	1
Yb-TiO_2 -Au	3.8	18	56	1
TiO_2 NW	2.8	15.3	48	1
TiO_2 NW-Au	2.7	15.2	46.3	1
Yb-TiO_2 NW-Au	3.2	17.7	54	1
Yb-TiO_2 NW-Au	2.6	14.3	46	1

Fig. 10. (a-b) PL emissions and their electron decay lifetimes of N719 dye loaded TiO_2, Yb-doped TiO_2, and Au NPs added Yb-doped TiO_2 NWS thin-films.

DSSC exhibits exceptional enhancement in photovoltaic properties.

3.6. Photovoltaic characteristics of DSSC under AM1.5G, 1 sun illuminatioan

Fig. 11(a) demonstrated the current density(*J*) vs voltage *(V)* parameters of DSSC. The associative photovoltaic parameters tabulated with the error analysis over four device sets are in Table. 4. Yb-doped TiO$_2$-based DSSC exhibit higher PCE% than undoped TiO$_2$. The enhanced PCE% can be attributed to the low recombination effect at the interface between dye molecules/TiO$_2$. As depicted in UPS, the engineered TiO$_2$ may have better Ohmic contact, and the formation of shallow traps improves the charge hopping. Moreover, incorporating Au NPs into the photoanode further increases PCE% with high current density(*J*). The improved (*J*) of Plasmon-induced DSSC can be attributed to the LSPR absorption band in conjunction with dye excitation. The DSSC with Au NPs added to Yb-doped TiO$_2$ exhibits a significantly higher PCE (η: 6.5 %), which is about 20 % greater than the test device's PCE (η: 5.3 %), and the nanowire clusters TiO$_2$ photoanode-based DSSC increases the PCE% up to 5.9 % with (Jsc) of 14.3 mA-cm^{-2}. The DSSC with Plasmonic Au NPs embedded Yb-doped TiO$_2$ NWs-DSSC exhibits a higher current density of 18.8 mA-cm^{-2} with a PCE% of 8 %. Specifically, the DSSC with a nanowire cluster structure yielded greater Jsc values due to the nanowires' greater surface-to-volume ratio, which facilitated enhanced dye molecule adsorption. Fig. 11(b) depicts the IPCE spectral response of the undoped and Yb-doped TiO$_2$ photoanode-based DSSC. The IPCE spectrum of the Yb-doped TiO$_2$/N719 photoanode-based DSSC is improved due to a favorable trapping system in the Yb-doped TiO$_2$ lattice, allowing for less recombination. Au NPs

Table 4

photovoltaic parameters of the Au NPs induced Plasmonic DSSC with nanowire cluster structured photoanode, tested under one sun (AM 1.5G) light illumination.

Photoanode	V$_{oc}$ (V)	J$_{sc}$ (mA-cm^{-2})	FF	η(%)
TiO$_2$	0.7 ± 0.03	12.16 ± 0.1	62 ± 1.2	5.3 ± 0.2
TiO$_2$:Au NPs	0.71 ± 0.05	14.3 ± 1.1	55 ± 2.3	5.6 ± 0.03
Yb-TiO$_2$	0.71 ± 0.1	13.7 ± 0.05	61 ± 0.6	6.1 ± 0.1
Yb-TiO$_2$: Au NPs	0.7 ± 0.04	14.4 ± 01.24	63 ± 3.9	6.55 ± 0.02
TiO$_2$ NW	0.71 ± 0.06	14 ± 0.9	59 ± 2.5	5.9 ± 0.05
TiO$_2$ NW: Au NPs	0.7 ± 0.05	15.7 ± 0.06	59 ± 3.2	6.38 ± 0.12
Yb-TiO$_2$ NW	0.7 ± 0	17 ± 0.2	63 ± 1.3	7.5 ± 0.09
Yb-TiO$_2$: NW Au NPs	0.72 ± 0.07	18.8 ± 0.04	59 ± 4	8 ± 0.21

Plasmon-induced DSSC had a more significant IPCE percentage, which refers to an increase in the optical density surrounding the metal surfaces in SPR-induced DSSC. As a result, more photons have been harvested[58]. The relative IPCE spectra ((ΔIPCE/IPCE) *100 %) are calculated to estimate the improvement in photo spectral response with the respective test device (TiO$_2$-based DSSC) under the influence of Yb-doping and Au NPs. Fig. 11(c) illustrates that the relative IPCE is distributed over 300nnm to 800 nm range. Particularly, the intensity of the IPCE spectrum from 400 nm to 600 nm is increased for Au NPs embedded TiO$_2$ and Au-embedded Yb-doped TiO$_2$. The improvement in the IPCE spectrum is attributable to the LSPR effect of Au NPs at 520 nm (Fig. 7)[81,82]. With the doping effect of Yb^{3+}, the extended relative IPCE spectra in the IR region demonstrate enhanced charge collection. Table S1 (in Supplmentary information) presents a comparative performance of Au NPs Plasmon induced Yb-doped TiO$_2$@ Au NPs/N719
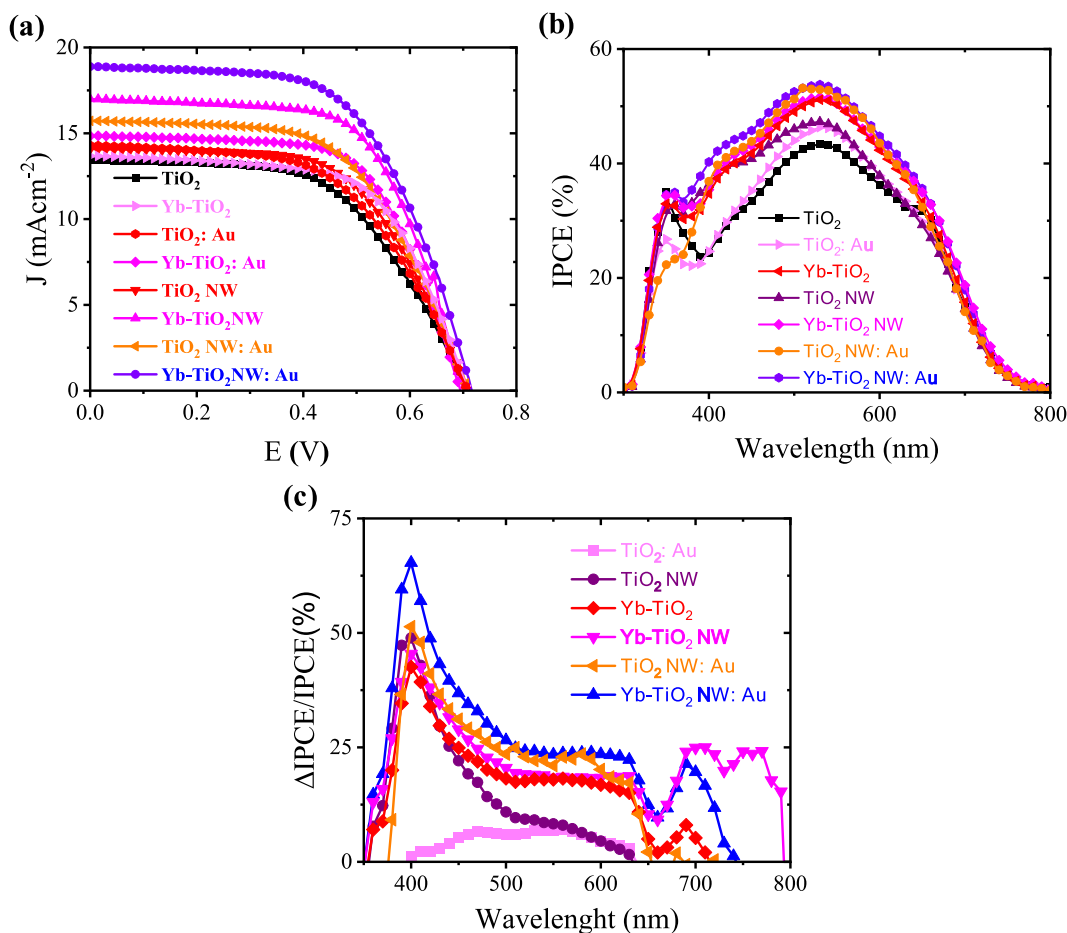

Fig. 11. (a). *J.* vs *V* plot, (b) IPCE spectral response, and (c) Relative changes in the IPCE spectral response of DSSC with nanostructured TiO$_2$, Yb-doped TiO$_2$, and Au NPs embedded Yb-doped TiO$_2$ photoanodes.

dye photoanode based DSSC vis-à-vis to various similar system from literature.

3.7. Indoor light photovoltaic (IPV) applications

The DSSC was then tested under indoor lighting conditions, while its optimal photovoltaic characteristics were monitored under (outdoor) AM 1.5G (1sun, 100 mW/cm^2) illumination. The light intensity is set for indoor light conditions to 1000LUX(327 μW/cm^2) using a white LED light source[7]. The ruthenium dye-sensitized solar cells have presented better results than thin-film and Si-based solar cells in indoor light conditions [83,84]. Fig. 12(a) presents the ruthenium(N719) dye absorption spectrum that overlaps with the spectral response of AM 1.5G and the white LED source. It was observed that the spectral response of LED was completely merged with the absorption spectrum of N719 dye molecules. Therefore, the DSSC could effectively generate more no excitations under LED illumination, thereby improving the photovoltaic properties.

Fig. 12(b) depicts the J-V characteristics of DSSC under White LED illumination with different nanostructured TiO$_2$ and Yb-TiO$_2$ photoanodes. Whereas Yb-doped TiO$_2$ employed DSSC reported with higher efficiency than pristine TiO$_2$ photoanodes, the corresponding parameters are tabulated in Table 5. With the addition of Plasmonic Au NPs, the DSSC was extended further into a higher PCE% of 11.2 %. Consequently, the Au/Yb-TiO$_2$ NW/dye photoanode increased the PCE% by more than 65 percent, and greatly enhancing photocurrent density compared to the test device.

3.8. EIS-Nyquist plots of DSSC

Electrochemical impedance spectroscopy (EIS) studies were used to characterize the interfacial charge transport resistance of the device. The EIS-Nyquist plot was performed under a frequency range of 1 MHz to 0.1 Hz, and an open-circuit voltage of 0.7 V under illumination by a White LED light source. Fig. 13 shows the Nyquist plot of DSSC, representing three depressed semicircles. The pertinent equivalent circuit was used to fit the Nyquist plot and extract the EIS parameters, as shown in Fig. 11(inset). In contrast, the first semicircle at high frequency is attributed to charge transfer resistance(R_2) at the counter electrode/electrolyte interface. The mid-range frequency semicircle represents the charge recombination resistance (R_3) at the TiO$_2$ photoanode/electrolyte interface. The third semicircle at a lower frequency is related to the Warburg diffusion resistance of electrolytes [85,86]. The distance between the origin and the Nyquist plot starting point on the left side indicates the series resistance (R_1). Table 6 lists the EIS parameters that were computed from the Nyquist plot. In contrast, the series resistance

Table 5
photovoltaic parameters of the constructed DSSC under white LED (1000 LUX, 327 μW/cm^2) illumination.

Photoanode	V_{oc} (V)	J_{sc} (μA-cm^{-2})	FF	η(%)
TiO$_2$	0.56 ± 0.01	135 ± 2.1	37 ± 0.2	8.6 ± 0.1
Yb-TiO$_2$	0.58 ± 0.002	129 ± 3.4	48 ± 0.4	11.15 ± 0.3
Yb-TiO$_2$: Au NPs	0.59 ± 0.01	155 ± 1.6	47 ± 3.7	13.3 ± 0.12
TiO$_2$ NW	0.565 ± 0.03	144 ± 5.9	40 ± 3.3	9.82 ± 0.5
Yb-TiO$_2$: NW	0.59 ± 0.01	148 ± 4.0	42 ± 2.1	11.4 ± 0.5
Yb-TiO$_2$: NW Au NPs	0.59 ± 0	153 ± 3.2	50 ± 0.1	13.95 ± 0.3

of (R_1) is identical across all devices, indicating that the components used to assemble the devices were optimized. R_2 and R_3 were exceptionally high in pristine TiO$_2$ (R_2:425 Ω and R_3:701 Ω, respectively). Yb-dopant and Au NPs influenced DSSC showed the lower interfacial resistances. Consequently, the charge transport is improved, which is crucial for enhanced photovoltaic characteristics. Specifically, Au NPs embedded Yb-doped TiO$_2$ NW exhibited the lowest charge transport resistance (R_2:86 Ω) and charge recombination resistance (R_3:20 Ω). These results were consistent with the J-V characteristics.

3.9. LSPR-induced DSSC

Fig. 14 displays the schematic representation of Plasmon-induced Yb-doped TiO$_2$ photoanode-based DSSC and the photoelectron generation/transport prospects. In this device, the dye molecules generate the electron/hole (e$^-$/h$^+$) pairs by absorbing the photons. Simultaneously, the Au NPs embedded in TiO$_2$ generate the (e$^-$/h$^+$) by creating a strong electric field around the Au NPs. This electric field is attributable to near-field effects with a penetration depth of up to 10 nm [87]. In contrast, due to the interaction with the Au NPs, the fermi level of TiO$_2$ is lowered to match the fermi energy level of Au NPs. And this down-shifted fermi level is able to enhance the charge injection efficiency from the dye molecules to the TiO$_2$ conduction band. Similarly, Under the influence of the Yb-dopant, the fermi level shifted down due to the formation of trap sites, as demonstrated in the UPS analysis, and these modified energy levels and formation of trap states are beneficial for charge transportation and injection at the interface with dye molecules. Thus, the high PCE% of Plasmon-induced DSSC is attributable to the combined LSPR absorption/scattering effect and defect-tuned energy band of Yb-doped TiO$_2$.

4. Conclusion

In conclusion, we have demonstrated the ensuing way to improve the PCE% by tuning the band structure of TiO$_2$ under the influence of Yb-
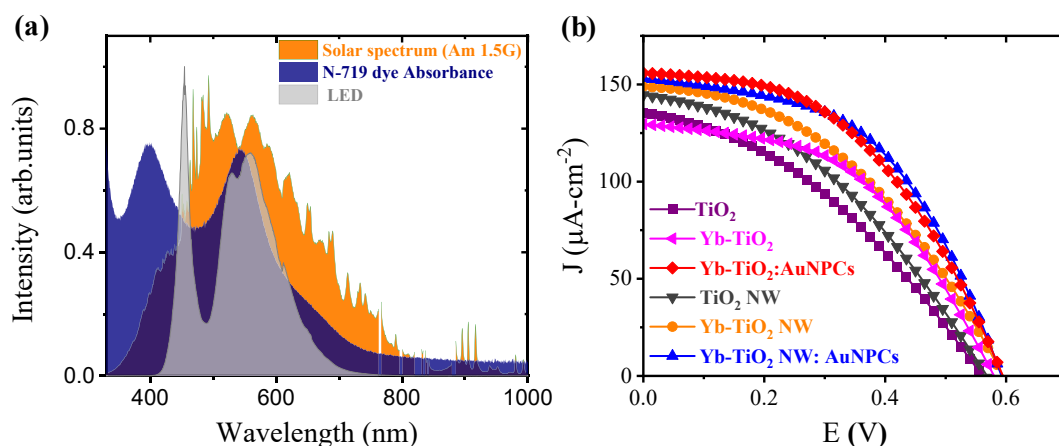

Fig. 12. (a) Spectral overlapping of the absorption spectrum of N719 dye molecules with the irradiance and emission spectrum of solar light (Am 1.5G), and White LED light, (b) J - V characteristic plots under Indoor light (White LED, 327 μW/cm^2) at ambient condition.
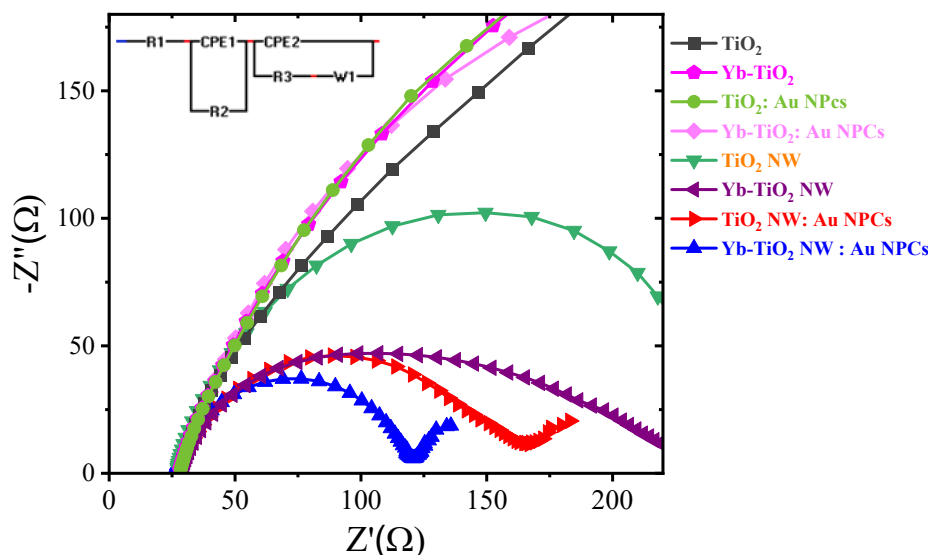
Fig. 13. Nyquist plots of DSSC based on various nanostructured TiO$_2$, Yb-doped TiO$_2$, and Au NPs embedded Yb-doped TiO$_2$ photoanodes.

Table 6
EIS parameters of TiO$_2$, Yb-doped TiO$_2$, and Au NPs added Yb-doped TiO$_2$ photoanodes applied DSSC under white LED (30 mW/cm^2) illumination.

Photoanode	$R_1(\Omega)$	$R_2(\Omega)$	$R_3(\Omega)$
TiO$_2$	24	425	701
Yb-TiO$_2$	30	129	606
TiO$_2$: Au NPs	21	556	333
Yb-TiO$_2$: Au NPs	27	418	297
TiO$_2$ NW	26	40	150
Yb-TiO$_2$: NW	29	74	109
TiO$_2$: NW Au NPs	28	104	29
Yb-TiO$_2$: NW Au NPs	26	86	20

dopant, plasmonic Au NPs. Plasmonic-induced DSSC with Au NPs added Yb-doped TiO$_2$ NW have constructed and executed with tremendous PCE%. Here, we have synthesized Yb-doped TiO$_2$ nanowire clusters and utilized them for photoanode fabrication. With the XRD, Raman, XPS, FESEM-EDX, and TEM analysis, we have confirmed the successful doping effect of Yb into TiO$_2$ lattice with improved properties. The Rietveld refinement analysis has shown the reduced lattice parameters

of 'a' and 'c' for Yb-doped TiO$_2$, which evidence the site substitution of Ti^{4+} with Yb^{3+}. Crystallite size & its distribution, variation in the phase transformations, and elemental composition & the formation of defect sites in the TiO$_2$ lattice were demonstrated in this work. Furthermore, dielectric characteristics illustrate the improved polarizability and electrical conductivity with the effect of Yb-doping. Likewise, the absorption peaks were found to be redshifted and identified with the reduced bandgap for Yb-doped TiO$_2$. By integrating the UV–vis and UPS analysis, the shallow trap states have been observed below the conduction band of TiO$_2$ by doping with Yb-intermediate energy states, which effectively improved the charge hopping mechanism and enhanced the photovoltaic properties of DSSC. PL quenching effects and short lifetime decay values ascribe efficient charge transportation/injection properties. Au NPs added to Yb-doped TiO$_2$ showed enhanced charge injection capabilities with dye molecules. Upon exposure to light, the electrons get excited and jump at the semiconductor/metallic nanoparticle interface, bringing the Fermi levels of TiO$_2$ and Au NPs into alignment. The downshifted fermi level of the Au-embedded Yb-doped TiO$_2$ enables the successful injection of charge from the dye molecules, as indicated by the PL quenching effect. As a result, the photovoltaic
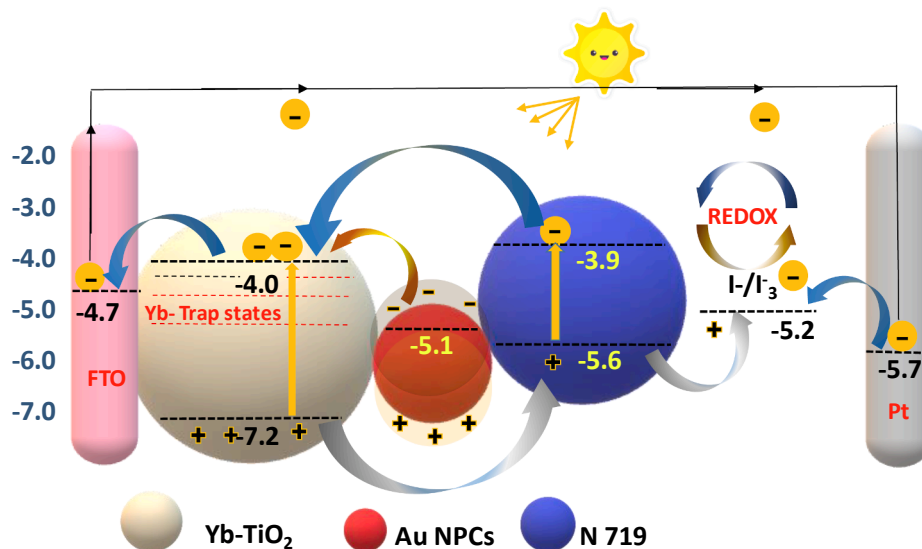

Fig. 14. Schematic representation of Plasmonic induced DSSC working.

properties were essentially enhanced by the influence of Yb-dopant and Au NPs. In contrast, Au NPs embedded Yb-doped TiO_2 photoanode-based DSSC exhibits a 20 % higher PCE% than the reference device (5.3 %). Additionally, when nanowire cluster structures are used in place of nanoparticles in the photoanode design, the PCE increases by more than 40 % compared to the test device. The Au-added Yb-TiO_2 NW performed well for indoor light conditions, with a PCE enhancement of roughly 52 % above undoped TiO_2 (η: 8.6 %). The enhancement in the light-harvesting abilities of DSSC was consistent with the IPCE spectral response. The EIS-Nyquist showed the decreased interfacial charge transport resistance for Plasmonic DSSC employed with Au-embedded Yb-TiO_2 nanowire clusters. As a result, the findings demonstrate a unique approach for enhancing the absorption capacity of TiO_2 by including rare-earth + 3 oxidized Yb(III) and Plasmonic Au NPs to harvest more solar energy.

CRediT authorship contribution statement

Venkata Seshaiah Katta: Data curation, Formal analysis, Investigation, Validation, Writing – review & editing, Writing – original draft. **V.R. Chappidi:** Formal analysis, Investigation, Validation, Methodology, Writing – original draft, Writing – review & editing. **Sai Santhosh Kumar Raavi:** Conceptualization, Resources, Funding acquisition, Supervision, Formal analysis, Investigation, Validation, Methodology, Writing – original draft, Writing – review & editing.

Declaration of Competing Interest

The authors declare that they have no known competing financial interests or personal relationships that could have appeared to influence the work reported in this paper.

Data availability

Data will be made available on request.

Acknowledgements

Appendix A. Supplementary material

Supplementary data to this article can be found online at https://doi.org/10.1016/j.apsusc.2022.155728.

References

[1] Y. Zhan, Y. Mei, L. Zheng, Materials capability and device performance in flexible electronics for the Internet of Things, J. Mater. Chem. C 2 (2014) 1220–1232.
[2] L. Liu, Q. Shi, C. Lee, A novel hybridized blue energy harvester aiming at all-weather IoT applications, Nano Energy 76 (2020), 105052.
[3] M. Prauzek, J. Konecny, M. Borova, K. Janosova, J. Hlavica, P. Musilek, Energy harvesting sources, storage devices and system topologies for environmental wireless sensor networks: a review, Sensors 18 (2018) 2446.
[4] A.T. Vicente, A. Araújo, M.J. Mendes, D. Nunes, M.J. Oliveira, O. Sanchez-Sobrado, et al., Multifunctional cellulose-paper for light harvesting and smart sensing applications, J. Mater. Chem. C 6 (2018) 3143–3181.
[5] I. Mathews, S.N. Kantareddy, T. Buonassisi, I.M. Peters, Technology and market perspective for indoor photovoltaic cells, Joule 3 (2019) 1415–1426.
[6] P.-T. Hsiao, W.-T. Hung, Y.-C. Chen, L.-K. Huang, C.-C. Chang, C.-F. Chen, et al., Pilot operation and lifetime assessment for indoor light energy harvesting photovoltaics, Renewable Energy 152 (2020) 67–74.
[7] A. Venkateswararao, J.K. Ho, S.K. So, S.-W. Liu, K.-T. Wong, Device characteristics and material developments of indoor photovoltaic devices, Mater. Sci. Eng.: R: Reports 139 (2020), 100517.
[8] S.O. Abdellatif, S. Josten, A.S. Khalil, D. Erni, F. Marlow, Transparency and diffused light efficiency of dye-sensitized solar cells: tuning and a new figure of merit, IEEE J. Photovoltaics 10 (2020) 522–530.
[9] H. Michaels, M. Rinderle, R. Freitag, I. Beneseri, T. Edvinsson, R. Socher, et al., Dye-sensitized solar cells under ambient light powering machine learning: towards autonomous smart sensors for the internet of things, Chem. Sci. 11 (2020) 2895–2906.
[10] H.S. Ryu, S.Y. Park, T.H. Lee, J.Y. Kim, H.Y. Woo, Recent progress in indoor organic photovoltaics, Nanoscale 12 (2020) 5792–5804.
[11] L.-K. Ma, Y. Chen, P.C. Chow, G. Zhang, J. Huang, C. Ma, et al., High-efficiency indoor organic photovoltaics with a band-aligned interlayer, Joule 4 (2020) 1486–1500.
[12] Z. Li, J. Zhang, S. Wu, X. Deng, F. Li, D. Liu, et al., Minimized surface deficiency on wide-bandgap perovskite for efficient indoor photovoltaics, Nano Energy 78 (2020), 105377.
[13] H. Sun, K. Deng, Y. Jiang, J. Ni, J. Xiong, L. Li, Realizing stable Artificial photon energy harvesting based on perovskite solar cells for diverse applications, Small 16 (2020) 1906681.
[14] P. Mazierski, A. Mikolajczyk, B. Bajorowicz, A. Malankowska, A. Zaleska-Medynska, J. Nadolna, The role of lanthanides in TiO2-based photocatalysis: a review, Appl. Catal. B 233 (2018) 301–317.
[15] Q. Guo, J. Wu, Y. Yang, X. Liu, W. Sun, Y. Wei, et al., Low-temperature processed rare-earth doped brookite TiO2 scaffold for UV stable, hysteresis-free and high-performance perovskite solar cells, Nano Energy 77 (2020), 105183.
[16] M. Khan, A. Suleman, M. Hasan, S. Ali, T.I. Al-Muhimeed, A.A. AlObaid, et al., Effect of Ce doping on the structural, optical, and photovoltaic properties of TiO2 based dye-sensitized solar cells, Mater. Chem. Phys. 274 (2021), 125177.
[17] K.L. Reddy, S. Kumar, A. Kumar, V. Krishnan, Wide spectrum photocatalytic activity in lanthanide-doped upconversion nanophosphors coated with porous TiO2 and Ag-Cu bimetallic nanoparticles, J. Hazard. Mater. 367 (2019) 694–705.
[18] R. Shashanka, H. Esgin, V.M. Yilmaz, Y. Caglar, Fabrication and characterization of green synthesized ZnO nanoparticle based dye-sensitized solar cells, J. Sci.: Adv. Mater. Devices 5 (2020) 185–191.
[19] B. Bajorowicz, M. Kobylański, A. Malankowska, P. Mazierski, J. Nadolna, A. Pieczyńska, et al., Application of metal oxide-based photocatalysis, 2018.
[20] V.S. Katta, V.R. Chappidi, S.S.K. Raavi, Samarium-doped TiO2 photoanodes for the molecular devices for solar energy conversion, Photonics Energy (2021) 6–15.
[21] L. Zhang, J.M. Cole, Anchoring groups for dye-sensitized solar cells, ACS Appl. Mater. Interfaces 7 (2015) 3427–3455.
[22] V.S. Katta, M. Velpandian, V.R. Chappidi, M.S. Ahmed, A. Kumar, S. Asthana, et al., Er3+ doped titania photoanode for enhanced performance of photo-electrochemical water splitting devices, Mater. Lett. 302 (2021) 130297.
[23] H. Ran, J. Fan, X. Zhang, J. Mao, G. Shao, Enhanced performances of dye-sensitized solar cells based on Au-TiO2 and Ag-TiO2 plasmonic hybrid nanocomposites, Appl. Surf. Sci. 430 (2018) 415–423.
[24] D. Liu, S. Li, P. Zhang, Y. Wang, R. Zhang, H. Sarvari, et al., Efficient planar heterojunction perovskite solar cells with Li-doped compact TiO2 layer, Nano Energy 31 (2017) 462–468.
[25] A. Agresti, S. Pescetelli, A.L. Palma, A.E. Del Rio Castillo, D. Konios, G. Kakavelakis, et al., Graphene interface engineering for perovskite solar modules: 12.6% power conversion efficiency over 50 cm2 active area, ACS Energy Lett. 2 (2017) 279–287.
[26] G. Yin, J. Ma, H. Jiang, J. Li, D. Yang, F. Gao, et al., Enhancing efficiency and stability of perovskite solar cells through Nb-doping of TiO2 at low temperature, ACS Appl. Mater. Interfaces 9 (2017) 10752–10758.
[27] X. Liu, Z. Liu, B. Sun, X. Tan, H. Ye, Y. Tu, et al., 17.46% efficient and highly stable carbon-based planar perovskite solar cells employing Ni-doped rutile TiO2 as electron transport layer, Nano Energy 50 (2018) 201–211.
[28] A. Chakraborty, G.H. Debnath, N.R. Saha, D. Chattopadhyay, D.H. Waldeck, P. Mukherjee, Identifying the correct host–guest combination to sensitize trivalent lanthanide (guest) luminescence: titanium dioxide nanoparticles as a model host system, J. Phys. Chem. C 120 (2016) 23870–23882.
[29] J. Day, S. Senthilarasu, T.K. Mallick, Improving spectral modification for applications in solar cells: a review, Renewable Energy 132 (2019) 186–205.
[30] A.K. Kaliamurthy, H.C. Kang, F.K. Asiam, K. Yoo, J.-J. Lee, Trap-assisted transition energy levels of SrF2: Pr3+– Yb3+ nanophosphor in TiO2 photoanode for luminescence tuning in dye-sensitized photovoltaic cells, Solar RRL 5 (2021) 2100411.
[31] P. Sehgal, A.K. Narula, Improved optical, electrochemical and photovoltaic properties of dye-sensitized solar cell composed of rare earth-doped zinc oxide, J. Mater. Sci.: Mater. Electron. 32 (2021) 16612–16622.
[32] V.S. Katta, A. Das, G. Cilaveni, S. Pulipaka, G. Veerappan, E. Ramasamy, et al., Vacancies induced enhancement in neodymium doped titania photoanodes based sensitized solar cells and photo-electrochemical cells, Sol. Energy Mater. Sol. Cells 220 (2021), 110843.
[33] R.N. Perumal, G. Subalakshmi, Near-infrared down-conversion in Yb3+: TiO2 for solar cell applications, J. Mater. Sci.: Mater. Electron. 28 (2017) 1837–1843.
[34] J.B. Pérez, M. Courel, M. Pal, F.P. Delgado, N. Mathews, Effect of ytterbium doping concentration on structural, optical and photocatalytic properties of TiO2 thin films, Ceram. Int. 43 (2017) 15777–15784.

[35] I. Padilla-Rosales, R. López-Juárez, G. López-Pacheco, C. Falcony, F. González, Near infrared photon-downshifting in Yb3+-doped titanates: the influence of intrinsic defects, J. Alloy. Compd. 834 (2020), 155081.

[36] M.S. Hamed, M.A. Adedeji, G.T. Mola, Rare-earth metal-induced plasmon resonances for enhanced photons harvesting in inverted thin film organic solar cell, Energy Fuels 35 (2021) 15010–15017.

[37] P. Kar, T.K. Maji, P.K. Sarkar, S. Sardar, S.K. Pal, Direct observation of electronic transition–plasmon coupling for enhanced electron injection in dye-sensitized solar cells, RSC Adv. 6 (2016) 98753–98760.

[38] I. Ibrahim, H. Lim, N. Wan, N. Huang, S. Lim, W. Busayaporn, et al., Plasmonic silver sandwich structured photoanode and reflective counter electrode enhancing power conversion efficiency of dye-sensitized solar cell, Sol. Energy 215 (2021) 403–409.

[39] H. Li, K. Yuan, Y. Zhang, J. Wang, Synthesis of Au-SiO2 asymmetric clusters and their application in ZnO nanosheet-based dye-sensitized solar cells, ACS Appl. Mater. Interfaces 5 (2013) 5601–5608.

[40] M. Ihara, K. Tanaka, K. Sakaki, I. Honma, K. Yamada, Enhancement of the absorption coefficient of cis-(NCS) 2 Bis (2, 2 '-bipyridyl-4, 4 '-dicarboxylate) ruthenium (II) Dye in Dye-Sensitized solar cells by a silver island film, J. Phys. Chem. B 101 (1997) 5153–5157.

[41] S. Chang, Q. Li, X. Xiao, K.Y. Wong, T. Chen, Enhancement of low energy sunlight harvesting in dye-sensitized solar cells using plasmonic gold nanorods, Energy Environ. Sci. 5 (2012) 9444–9448.

[42] H. Choi, W.T. Chen, P.V. Kamat, Know thy nano neighbor. Plasmonic versus electron charging effects of metal nanoparticles in dye-sensitized solar cells, ACS Nano 6 (2012) 4418–4427.

[43] J. Qi, X. Dang, P.T. Hammond, A.M. Belcher, Highly efficient plasmon-enhanced dye-sensitized solar cells through metal@ oxide core–shell nanostructure, ACS Nano 5 (2011) 7108–7116.

[44] P. Rai, Plasmonic noble metal@ metal oxide core–shell nanoparticles for dye-sensitized solar cell applications, Sustainable Energy Fuels 3 (2019) 63–91.

[45] M. Dissanayake, J. Kumari, G. Senadeera, C. Thotawatthage, Efficiency enhancement in plasmonic dye-sensitized solar cells with TiO2 photoanodes incorporating gold and silver nanoparticles, J. Appl. Electrochem. 46 (2016) 47–58.

[46] S. Sreeja, B. Pesala, Plasmonic enhancement of betanin-lawsone co-sensitized solar cells via tailored bimodal size distribution of silver nanoparticles, Sci. Rep. 10 (2020) 1–17.

[47] Y.-Z. Zheng, H. Ding, Y. Liu, X. Tao, G. Cao, J.-F. Chen, In situ hydrothermal growth of hierarchical ZnO nanourchin for high-efficiency dye-sensitized solar cells, J. Power Sources 254 (2014) 153–160.

[48] Q. Zhang, C.S. Dandeneau, X. Zhou, G. Cao, ZnO nanostructures for dye-sensitized solar cells, Adv. Mater. 21 (2009) 4087–4108.

[49] C. Li, Y. Huang, C. Chen, X. Feng, Z. Zhang, High-performance polymer electrolyte membrane modified with isocyanate-grafted Ti3+ doped TiO2 nanowires for lithium batteries, Appl. Surf. Sci. 563 (2021), 150248.

[50] T. Luttrell, S. Halpegamage, J. Tao, A. Kramer, E. Sutter, M. Batzill, Why is anatase a better photocatalyst than rutile?-Model studies on epitaxial TiO2 films, Sci. Rep. 4 (2014) 1–8.

[51] P. Gnida, P. Jarka, P. Chulkin, A. Drygała, M. Libera, T. Tański, et al., Impact of TiO2 nanostructures on dye-sensitized solar cells performance, Materials 14 (2021) 1633.

[52] M. Kumari, C. Perera, B. Dassanayake, M. Dissanayake, G. Senadeera, Highly efficient plasmonic dye-sensitized solar cells with silver nanowires and TiO2 nanofibres incorporated multi-layered photoanode, Electrochim. Acta 298 (2019) 330–338.

[53] F. Xu, Y. Sun, H. Gao, S. Jin, Z. Zhang, H. Zhang, et al., High-performance perovskite solar cells based on NaCsWO3@ NaYF4@ NaYF4: Yb, Er upconversion nanoparticles, ACS Appl. Mater. Interfaces 13 (2021) 2674–2684.

[54] F. Qiao, Y. Xie, G. He, H. Chu, W. Liu, Z. Chen, Light trapping structures and plasmons synergistically enhance the photovoltaic performance of full-spectrum solar cells, Nanoscale 12 (2020) 1269–1280.

[55] J.-C.G. Bünzli, A.-S. Chauvin, Lanthanides in solar energy conversion, in: Handbook on the Physics and Chemistry of Rare Earths, vol. 44, ed: Elsevier, 2014, pp. 169–281.

[56] T. Liu, X. Bai, C. Miao, Q. Dai, W. Xu, Y. Yu, et al., Yb2O3/Au upconversion nanocomposites with broad-band excitation for solar cells, J. Phys. Chem. C 118 (2014) 3258–3265.

[57] N. Yao, J. Huang, K. Fu, X. Deng, M. Ding, X. Xu, Rare earth ion doped phosphors for dye-sensitized solar cells applications, RSC Adv. 6 (2016) 17546–17559.

[58] P. Zhao, Y. Zhu, X. Yang, X. Jiang, J. Shen, C. Li, Plasmon-enhanced efficient dye-sensitized solar cells using core–shell-structured β-NaYF 4: Yb, Er@ SiO 2@ Au nanocomposites, J. Mater. Chem. A 2 (2014) 16523–16530.

[59] P. Ramasamy, J. Kim, Combined plasmonic and upconversion rear reflectors for efficient dye-sensitized solar cells, Chem. Commun. 50 (2014) 879–881.

[60] J.V. Vaghasiya, K.K. Sonigara, L. Suresh, M. Panahandeh-Fard, S.S. Soni, S.C. Tan, Efficient power generating devices utilizing low intensity indoor lights via non-radiative energy transfer mechanism from organic ionic redox couples, Nano Energy 60 (2019) 457–466.

[61] C. Hora, F. Santos, M.G.F. Sales, D. Ivanou, A.l. Mendes, Dye-sensitized solar cells for efficient solar and artificial light conversion, ACS Sustainable Chem. Eng. 7 (2019) 13464–13470.

[62] Y. Cui, Y. Wang, J. Bergqvist, H. Yao, Y. Xu, B. Gao, et al., Wide-gap non-fullerene acceptor enabling high-performance organic photovoltaic cells for indoor applications, Nat. Energy 4 (2019) 768–775.

[63] H.K. Lee, Z. Li, J.R. Durrant, W.C. Tsoi, Is organic photovoltaics promising for indoor applications? Appl. Phys. Lett. 108 (2016), 253301.

[64] V.S. Katta, C. Biswas, S.S.K. Raavi, Tunable broadband NIR PL emissions with (Nd3+/Er3+) codoped TiO2 via synergetic energy transfer, ACS App. Opt. Mater. (2022).

[65] J. Zhang, L. Xu, Z. Zhu, Q. Liu, Synthesis and properties of (Yb, N)-TiO2 photocatalyst for degradation of methylene blue (MB) under visible light irradiation, Mater. Res. Bull. 70 (2015) 358–364.

[66] M. Zikriya, Y. Nadaf, P.V. Bharathy, C. Renuka, Luminescent characterization of rare earth Dy3+ ion doped TiO2 prepared by simple chemical co-precipitation method, J. Rare Earths 37 (2019) 24–31.

[67] R. Hernández, J.R. Hernández-Reséndiz, A. Martínez-Chávez, R. Velázquez-Castillo, L. Escobar-Alarcón, K. Esquivel, X-ray diffraction Rietveld structural analysis of Au–TiO2 powders synthesized by sol–gel route coupled to microwave and sonochemistry, J. Sol-Gel Sci. Technol. 95 (2020) 239–252.

[68] H.A. Yurtsever, M. Çiftçioğlu, The effect of rare earth element doping on the microstructural evolution of sol-gel titania powders, J. Alloy. Compd. 695 (2017) 1336–1353.

[69] R. Dominguez, G. Alarcón-Flores, M. Aguilar-Frutis, R. Sánchez-Alarcón, C. Falcony, H. Dorantes-Rosales, et al., Effect on the stabilization of the anatase phase and luminescent properties of samarium-doped TiO2 nanocrystals prepared by microwave irradiation, J. Alloy. Compd. 687 (2016) 121–129.

[70] Z. Rao, X. Xie, X. Wang, A. Mahmood, S. Tong, M. Ge, et al., Defect chemistry of Er3+-doped TiO2 and its photocatalytic activity for the degradation of flowing gas-phase VOCs, J. Phys. Chem. C 123 (2019) 12321–12334.

[71] X.-X. Gao, Q.-Q. Ge, D.-J. Xue, J. Ding, J.-Y. Ma, Y.-X. Chen, et al., Tuning the fermi-level of TiO 2 mesoporous layer by lanthanum doping towards efficient perovskite solar cells, Nanoscale 8 (2016) 16881–16885.

[72] X. Luo, S. Zhu, J. Wang, C. Wang, M. Wu, Characterization and computation of Yb/TiO2 and its photocatalytic degradation with benzohydroxamic acid, Int. J. Environ. Res. Public Health 14 (2017) 1471.

[73] A. Saha, A. Moya, A. Kahnt, D. Iglesias, S. Marchesan, R. Wannemacher, et al., Interfacial charge transfer in functionalized multi-walled carbon nanotube@ TiO 2 nanofibres, Nanoscale 9 (2017) 7911–7921.

[74] L. Shi, C. Xu, X. Sun, H. Zhang, Z. Liu, X. Qu, et al., Facile fabrication of hierarchical BiVO4/TiO2 heterostructures for enhanced photocatalytic activities under visible-light irradiation, J. Mater. Sci. 53 (2018) 11329–11342.

[75] M. Zare, A. Mortezaali, A. Shafiekhani, Photoelectrochemical determination of shallow and deep trap states of platinum-decorated TiO2 nanotube arrays for photocatalytic applications, J. Phys. Chem. C 120 (2016) 9017–9027.

[76] M.C. Joshi, R.K. Gupta, J. Prakash, Hydrothermal synthesis and Ta doping of TiO2 nanorods: effect of soaking time and doping on optical and charge transfer properties for enhanced SERS activity, Mater. Chem. Phys. 278 (2022), 125642.

[77] R. Selvapriya, V. Sasirekha, P. Vajeeston, J.M. Pearce, J. Mayandi, Reaction induced multifunctional TiO2 rod/particle nanostructured materials for screen printed dye sensitized solar cells, Ceram. Int. 47 (2021) 8094–8104.

[78] M. Tsega, F. Dejene, Influence of acidic pH on the formulation of TiO2 nanocrystalline powders with enhanced photoluminescence property, Heliyon 3 (2017) e00246.

[79] M.M. Hassan, W. Khan, A. Azam, A. Naqvi, Influence of Cr incorporation on structural, dielectric and optical properties of ZnO nanoparticles, J. Ind. Eng. Chem. 21 (2015) 283–291.

[80] Z. Wang, Y. Li, H. Chen, J. Fan, X. Wang, X. Ma, Correlation between the radius of acceptor ion and the dielectric properties of co-doped TiO2 ceramics, Ceram. Int. 45 (2019) 14625–14633.

[81] H.-J. Hwang, S.-J. Joo, S.A. Patil, H.-S. Kim, Efficiency enhancement in dye-sensitized solar cells using the shape/size-dependent plasmonic nanocomposite photoanodes incorporating silver nanoplates, Nanoscale 9 (2017) 7960–7969.

[82] H.-Y. Kim, H. Yoon, J.S. Suh, Surface plasmon-enhanced dye-sensitized solar cells based on double-layered composite films consisting of TiO 2/Ag and TiO 2/Au nanoparticles, RSC Adv. 5 (2015) 27464–27469.

[83] S. Sasidharan, A. Jagadeesh, S.C. Pradhan, B.N. Nair, A.A.P. Mohamed, K.N. Unni, et al., ZnO hierarchical structures as sacrificial inclusions for enhanced performance under full sun and indoor light in bifacial dye sensitized solar cells, Sol. Energy 226 (2021) 214–224.

[84] Y.S. Tingare, N.S.n. Vinh, H.H. Chou, Y.C. Liu, Y.S. Long, T.C. Wu, et al., New acetylene-bridged 9, 10-conjugated anthracene sensitizers: application in outdoor and indoor dye-sensitized solar cells, Adv. Energy Mater. 7 (2017) 1700032.

[85] J.-D. Peng, H.-H. Lin, C.-T. Lee, C.-M. Tseng, V. Suryanarayanan, R. Vittal, et al., Hierarchically assembled microspheres consisting of nanosheets of highly exposed (001)-facets TiO 2 for dye-sensitized solar cells, RSC Adv. 6 (2016) 14178–14191.

[86] D.-K. Hwang, B. Lee, D.-H. Kim, R.P. Chang, Efficiency enhancement in dye-sensitized solar cells by three-dimensional photonic crystals, Appl. Phys Express 5 (2012), 122301.

[87] S. Bhardwaj, A. Pal, K. Chatterjee, T.H. Rana, G. Bhattacharya, S. Sinha Roy, et al., Fabrication of efficient dye-sensitized solar cells with photoanode containing TiO2–Au and TiO2–Ag plasmonic nanocomposites, J. Mater. Sci.: Mater. Electron. 29 (2018) 18209–18220.